Analytical calculation model for predicting cracking behavior of reinforced concrete ties

Tan, Reignard; Hendriks, Max A.N.; Geiker, Mette; Kanstad, Terje

Citation (APA)
Tan, R., Hendriks, M. A. N., Geiker, M., & Kanstad, T. (2020). Analytical calculation model for predicting cracking behavior of reinforced concrete ties. *Journal of Structural Engineering (United States)*, *146*(2), Article 04019206. https://doi.org/10.1061/(ASCE)ST.1943-541X.0002510

Important note
To cite this publication, please use the final published version (if applicable).
Please check the document version above.

1 **Analytical calculation model for predicting the cracking behavior of reinforced concrete**

2 **ties**

3

4 Author 1

5 • Reignard Tan*

6 • PhD candidate

7 • Department of Structural Engineering, Norwegian University of Science and

8   Technology, Trondheim, Norway.

9

10 Author 2

11 • Max A.N. Hendriks

12 • Professor

13 • Department of Structural Engineering, Norwegian University of Science and

14   Technology, Trondheim, Norway.

15 • Faculty of Civil Engineering & Geosciences, Delft University of Technology, Delft, The

16   Netherlands.

17

18 Author 3

19 • Mette Geiker

20 • Professor

21 • Department of Structural Engineering, Norwegian University of Science and

22   Technology, Trondheim, Norway.

23

24 Author 4

25 • Terje Kanstad

26 • Professor

27 • Department of Structural Engineering, Norwegian University of Science and

28   Technology, Trondheim, Norway.

29

30   * Corresponding author at: Multiconsult AS, Postboks 265 Skøyen, 0213 Oslo, Norway.

31   E-mail address: reignard.tan@multiconsult.no

32   Contact number: +4741561203

33

34   **Abstract**

35   This paper formulates an analytical calculation model for predicting the cracking behavior of

36   reinforced concrete ties to provide more consistent crack width calculation methods for large-

37   scale concrete structures in which large bar diameters and covers are used. The calculation

38   model was derived based on the physical behavior of reinforced concrete ties reported from

39   experiments and finite element analyses in the literature. The derivations led to a second order

40   differential equation for the slip that accounts for the 3D effects of internal cracking by using a

41   proper bond-slip law. The second order differential equation for the slip was solved completely

42   analytically, resulting in a closed-form solution in the case of lightly loaded members and in a

43   non-closed-form solution in the case of heavily loaded members. Finally, the paper provides a

44   solution strategy to facilitate a practical and applicable method for predicting the complete

45   cracking response. Comparison with experimental and finite element results in the literature

46   demonstrated the ability of the calculation model to predict crack widths and crack spacing

47   consistently and on the conservative side regardless of the bar diameter and cover.

48

52

1. Introduction

Predicting the cracking behavior of reinforced concrete (RC) structures consistently and accurately is not straightforward. This is reflected in the many approaches proposed in the literature (Borosnyói and Balázs 2005). Formulas based on empirical, semi-empirical, elastic analysis, and even fracture mechanics have all been proposed. Mechanical calculation models based on the internal cracking behavior of RC ties have also recently been proposed (Fantilli et al. 2007, Debernardi and Taliano 2016, Kaklauskas 2017).

The study presented in this paper is part of an ongoing research project with the overall objective of improving crack width calculation methods for the large-scale concrete structures planned for the coastal highway route "Ferry-free E39" in Norway. The Norwegian Public Roads Administration (NPRA) recommends that the design of such structures should follow the guidelines provided in N400 (NPRA 2015), which state that the crack width calculation methods should be in accordance with the provisions in Eurocode 2 (EC2) (CEN 2004). However, Tan et al. (2018a) showed that the crack width formulas recommended by EC2 and the *fib* Model Code 2010 (MC2010) (*fib* 2013) predict the cracking behavior of structural elements inconsistently, particularly in cases of large covers and bar diameters. The analytical calculation model presented in this paper was based on solving the second order differential equation (SODE) for the slip when applying a bond-slip law first proposed by Eligehausen et al. (1983) and later adopted by MC2010. Other authors in the literature have used a similar approach (e.g. Russo and Romano 1992, Balász 1993, Debernardi and Taliano 2016), an approach which has recently been acknowledged in the state-of-the-art French research project CEOS.fr (2016) as an alternative way of calculating crack widths for large RC members. The main drawback in using this approach until now was the analytically complex solution of the SODE for the slip, thus resorting to numerical solution techniques instead and by that reducing the practical applicability of the approach. Moreover, the background of the SODE for the slip was never properly elaborated.

The aim of this research was to provide more realistic and consistent surface crack width calculation methods for large-scale concrete structures, where large covers in combination with

83   large bar diameters in several layers and bundles are typically used, by deriving and solving the

84   SODE for the slip completely analytically. First, the SODE for the slip was derived. Then, the

85   SODE for the slip was solved analytically, after which a solution strategy for determining the

86   complete cracking response was developed for the purposes of practical application. Finally, the

87   application was demonstrated by comparing analytical predictions with experimental and finite

88   element (FE) results reported in the literature.

89

90   The analytical model was derived using the concept of axisymmetry and applies first and

91   foremost to such conditions. However, it will be shown that the model also has the ability to

92   predict the cracking behavior of RC ties that deviate from such conditions by transforming an

93   arbitrary cross section into an equivalent axisymmetric cross section. Moreover, predicting

94   realistic and consistent surface crack widths is an important part of the structural design, and it

95   might also be relevant for the aesthetics of a structure (Leonhardt 1988). On the other hand it is

96   often argued that the crack width at the reinforcement appears more relevant in terms of

97   durability. Predicting the latter, though, becomes rather complicated and was not addressed in

98   this study.

99

100   **2. The physical behavior of RC ties**

101   A typical deformation configuration of RC ties according to several experimental studies

102   reported in the literature (Watstein and Mathey 1959, Broms 1968, Husain and Ferguson 1968,

103   Yannopoulos 1989, Beeby 2004 and Borosnyói and Snóbli 2010) is depicted in Fig. 1(a). Note

104   that the crack width at the interface between concrete and steel $w_{cr,int}$ is considerably smaller

105   than that on the concrete surface w_{cr}, which according to Goto (1972) and Tammo and

106   Thelanderrson (2009) is due to the rib interaction between concrete and steel. This causes the

107   concrete to crack internally, which allows it to follow the displacement field of steel at the

108   interface almost completely. This reported physical behavior formed the basis for ignoring the

109   crack width at the interface in the FE model of Tan et al. (2018c). This imposed equal

110   longitudinal displacements for concrete and steel at the interface as shown in Fig. 1(b), in which

111   it should be noted that the crack width w_{cr} applies to the concrete surface only. The FE model

112   was validated against the classical experiments of Bresler and Bertero (1968) and Yannopoulos

113   (1989), where comparison of steel strains, the development of crack widths and the mean crack

114   spacing showed good agreement. Furthermore, the FE model was also used to analyze

115   cylindrical RC ties to better understand the cracking behavior. It was observed that the bond

116   transfer at the interface caused radial displacements of the concrete, which in turn increased

117   hoop stresses and strains. This resulted in internal splitting cracks and inclined cracks, depicted

118   respectively as circles and straight lines in Fig. 1(b), when the principal stresses exceeded the

119   tensile strength of the concrete. Moreover, deriving local bond-slip curves at different positions

120   over the bar length showed that such curves include the effect that internal splitting and inclined

121   cracks had on reducing the bond transfer. In other words, the local bond-slip curve describes

122   how the 3D behavior of an RC tie affects the bond transfer. This shows that a single local bond-

123   slip curve is sufficient to describe the mean bond transfer at the interface between concrete and

124   steel for an arbitrary RC tie.

125

126   **3. The mechanical crack width calculation model**

127   *3.1 Main assumptions*

128   The analytical calculation model was derived based on the physical behavior of RC ties

129   discussed in the previous section. However, some simplifications were made, and at first the

130   concept of axisymmetry was also used for simplicity. Firstly, concrete and steel were both

131   treated as elastic materials. Secondly, the nonlinearity of the internal cracking of the confining

132   concrete was accounted for by lumping this behavior to the interface between the materials

133   using a bond-slip law, i.e. claiming that the three sections in Fig. 2(a), (b) and (c) are statically

134   equivalent. Note that a physical slip u occurs at the interface in Fig. 2(b) and (c) as a result of

135   treating concrete and steel as elastic materials. This means that the total slip s_{tot} in the statically

136   equivalent section in Fig. 2(c) is composed of two parts: the slip at the interface u caused by the

137   formation of internal inclined cracks and the elastic deformations of the concrete caused by axial

138   and shear deformations in the cover s_s. This also conforms to the definition of slip in *fib* bulletin

139   10 (2000). Assuming that the slip at the interface is equivalent to the deformation caused by

140   internal inclined cracks implies in reality that the crack width at the interface can be ignored in

141   the calculation model, so that the resulting crack width applies to the concrete surface.

142   Furthermore, the Poisson's ratio for concrete can be ignored ($\nu_c = 0$) because the concrete is

143 assumed to be exposed to heavy internal cracking as described in the previous section. Finally,

144 the displacement field depicted in Fig. 3, which shows the deformed configuration of an arbitrary

145 section in an RC tie subjected to loading at the rebar ends, can be assumed to apply for an

146 arbitrary statically equivalent section.

147

148 The continuum concept (Irgens 2008) is hereafter used to formulate the compatibility, material

149 laws and equilibrium for concrete and steel.

150

151 ***3.2 Equations for concrete***

152 *3.2.1 General equations*

153 The SODE for the concrete displacements was derived by using the cylindrical coordinates and

154 the displacement field depicted in Fig. 3. Concrete strains at the interface ε_{ci} and the specimen

155 surface ε_{co} were assumed to be related as

156

$$\psi(x) = \frac{\varepsilon_{co}}{\varepsilon_{ci}} \leq 1 \tag{1}$$

157

158 in which

159

$$\varepsilon_{ci} = \frac{dw_{ci}(x)}{dx} \tag{2}$$

160 and

$$\varepsilon_{co} = \frac{dw_{co}(x)}{dx} \tag{3}$$

161

162 where dw_{ci} and dw_{co} are differential displacements at the interface and at the specimen surface

163 respectively. Note that the inequality in Eq. (1) is because the concrete strains at the specimen

164 surface cannot exceed the concrete strains at the interface as a consequence of force being

165 applied at the steel bar ends. The maximum longitudinal displacement of the concrete cover

166 relative to the concrete interface is

167

$$-\Delta w_{\text{cmax}}(x) = w_{\text{ci}}(x) - w_{\text{co}}(x) \tag{4}$$

168

169   Moreover, longitudinal concrete displacements can be formulated as

170

$$w_{\text{c}}(R, x) = w_{\text{ci}}(x) + \Delta w_{\text{cmax}}(x)\bar{\psi}(R, x) \tag{5}$$

171

172   in which $\bar{\psi}$ is a shape function describing the variation in longitudinal displacements over the

173   section and over the bar length. It was chosen to satisfy the following boundary conditions:

174

$$w_{\text{c}}(R_1, x) = w_{\text{ci}}(x)$$
$$w_{\text{c}}(R_2, x) = w_{\text{co}}(x) \tag{6}$$

175

176   where R_1 and R_2 are the radial coordinates of respectively the interface and the specimen

177   surface. It should be noted that Fig. 3 omits radial displacements for the concrete, while in the

178   case of axisymmetry displacements in the hoop direction are non-existent. Omitting radial

179   displacements contradicts the physical behavior of RC ties discussed previously, but using a

180   bond-slip law $\tau(u)$, with τ denoting the bond stress, will take into account the 3D-effects that are

181   excluded when radial displacements for the concrete are omitted. This means that Eq. (5)

182   suffices in describing the displacement field for concrete. Now, using Green strains for small

183   displacements yield the following non-zero components in the strain tensor for concrete:

184

$$\varepsilon_{\text{c}} = \frac{\partial w_{\text{c}}(R, x)}{\partial x} = \frac{dw_{\text{ci}}(x)}{dx} + \frac{\partial}{dx}[\Delta w_{\text{cmax}}(x)\bar{\psi}(R, x)] \tag{7}$$

185

$$\gamma_{\text{c}Rx} = \gamma_{\text{c}xR} = \frac{\partial w_{\text{c}}(R, x)}{\partial R} = \Delta w_{\text{cmax}}(x)\frac{d\bar{\psi}(R, x)}{dR} \tag{8}$$

186

187   where ε_{c} and $\gamma_{\text{c}Rx} = \gamma_{\text{c}xR}$ are longitudinal strains and engineering shear strains respectively.

188   Consequently, Eq. (7) and (8), and ignoring the Poisson's ratio for concrete, yield the following

189   non-zero components for the stress tensor:

190

$$\sigma_c = E_c \varepsilon_c \tag{9}$$

191

$$\tau_{cxR} = \tau_{cRx} = \frac{1}{2} E_c \gamma_{cxR} \tag{10}$$

192

193   where σ_c and $\tau_{cRx} = \tau_{cxR}$ are respectively the normal and the shear stresses, while E_c is the

194   Young's modulus for concrete. Considering equilibrium for the concrete in Fig. 2(c) yields

195

$$\frac{dF_c(x)}{dx} = \tau(u)\sum\pi\phi_s \tag{11}$$

196

197   where τ is the bond stress dependent on the slip at the interface u, and $\sum\pi\phi_s$ is the total

198   perimeter surrounding the steel bars in a cross section. The concrete force resultant can be

199   formulated as

200

$$F_c(x) = \int_{A_c} \sigma_c dA_c \tag{12}$$

201

202   where A_c is the concrete area.

203

204   Finally, inserting Eq. (12), (9), (7), (4), (1), (2) and (3) in Eq. (11) successively yields

205

$$E_c \frac{\partial}{\partial x} \int_{A_c} \left\{ \left(\frac{dw_{ci}(x)}{dx} - \frac{dw_{ci}(x)}{dx} [1 - \psi(x)] \bar{\psi}(R,x) \right. \right.$$
$$\left. \left. - [w_{ci}(x) - w_{co}(x)] \frac{\partial\bar{\psi}(R,x)}{\partial x} \right\} dA_c = \tau(u)\sum\pi\phi_s \tag{13}$$

206

207   which is the SODE for the longitudinal concrete displacements at the interface.

208

209   *3.2.2 Simplified equations*

210   An analytical solution of Eq. (13) is possible in the case of axisymmetry if both ψ and $\bar{\psi}$ are

211   known. In most practical situations, however, this is not the case. A practical approach to Eq.

212   (13) would therefore be to redefine Eq. (1) as

213

$$\psi(x) = \psi = \frac{\varepsilon_{cm}}{\varepsilon_{ci}} \leq 1 \tag{14}$$

214

215   in which

216

$$\varepsilon_{cm} = \frac{dw_{cm}(x)}{dx} = \psi\varepsilon_{ci} \tag{15}$$

217

218   are mean concrete strains and w_{cm} are mean displacements over the section, see Fig. 3, which

219   in this particular case simplifies the shape function to

220

$$\bar{\psi} = 1 \tag{16}$$

221

222   Note that ψ in Eq. (14) is now assumed constant. Edwards and Picard (1972) were the first to

223   introduce the concept of Eq. (14). This was later investigated more thoroughly by conducting

224   nonlinear finite element analysis (NLFEA) on cylindrical RC ties in Tan et al. (2018b). It was

225   concluded that although the shape function $\bar{\psi}$, first defined in Eq. (5) varied with respect to both

226   R and x-coordinates over the bar length, the ratio in Eq. (14) remained more or less constant

227   over the bar length except for a small region close to the loaded end. Actually, it was observed

228   that a constant value of $\psi = 0.70$ over the entire bar length seemed reasonable independent of

229   geometry and load level. The physical interpretation of Eq. (15) is that *plane sections that do not*

230   *remain plane* are implicitly accounted for in determining the equilibrium. Now, replacing w_{co} with

231   w_{cm} in Eq. (13) and inserting Eq. (14) and (16) simplifies the SODE for the longitudinal concrete

232   displacements at the interface to

233

$$\psi A_c E_c \frac{d^2 w_{ci}(x)}{dx^2} = \tau(u)\sum \pi\phi_s \tag{17}$$

234

235   ***3.3 Equations for steel***

236   Longitudinal displacements for steel were assumed uniform over its radius. And since the

237   Poisson's ratio for concrete was ignored and axisymmetry applied for circular steel rebars

238   means that Eq. (18)

239

$$w_s(R, x) = w_s(x) \tag{18}$$

240

241   suffices in describing the displacement field for steel. The following normal strain was thus the

242   only non-zero component in the strain tensor when Green strains for small deformations were

243   applied:

244

$$\varepsilon_s = \frac{dw_s(x)}{dx} \tag{19}$$

245

246   Moreover, the Poisson's ratio for steel was ignored ($v_s = 0$) as the lateral effects it had on bond

247   were assumed to be included in the bond-slip curve. This led to the following normal stress

248   being the only non-zero component in the stress tensor:

249

$$\sigma_s = E_s \varepsilon_s \tag{20}$$

250

251   where E_s is the Young's modulus for steel. The equilibrium of steel in Fig. 2(c) yields

252

$$\frac{dF_s(x)}{dx} = -\tau(u)\sum \pi \phi_s \tag{21}$$

253

254   Furthermore, the steel force resultant was obtained as

255

$$F_s(x) = \int_{A_s} \sigma_s dA_s = A_s E_s \frac{dw_s(x)}{dx} \tag{22}$$

256

257   when inserting Eq. (20) and (19) successively. Finally, inserting Eq. (22) in (21) yields

258

$$A_s E_s \frac{d^2 w_s(x)}{dx^2} = -\tau(u)\sum\pi\phi_s \qquad (23)$$

259

260 which is the SODE for the steel displacements.

261

262 **3.4 Compatibility**

263 The slip was defined in terms of the displacement field depicted in Fig. 3 as

264

$$-u(x) = w_s(x) - w_{ci}(x) \qquad (24)$$

265

266 Differentiating Eq. (24) once and inserting Eq. (2) and (19) provides the first derivative of the slip

267 as

268

$$-u'(x) = \frac{dw_s(x)}{dx} - \frac{dw_{ci}(x)}{dx} = \varepsilon_s - \varepsilon_{ci} \qquad (25)$$

269

270 **3.5 The second order differential equation for the slip**

271 Inserting Eq. (23) in (17) provides

272

$$\frac{d}{dx}\left[\frac{dw_{ci}(x)}{dx} + \xi\frac{dw_s(x)}{dx}\right] = 0 \qquad (26)$$

273

274 where

275

$$\xi = \frac{\alpha_e \rho_s}{\psi} \qquad (27)$$

276

$$\alpha_e = \frac{E_s}{E_c} \qquad (28)$$

277

278 and

279

$$\rho_s = \frac{A_s}{A_c} \tag{29}$$

280

281 Inserting Eq. (25) and (23) successively in Eq. (26) yields the SODE for the slip as

282

$$\frac{d^2 u(x)}{dx^2} - \chi \tau(u) = 0 \tag{30}$$

283

284 where

285

$$\chi = \frac{\sum \pi \phi_s}{A_s E_s}(1 + \xi) \tag{31}$$

286

287 By introducing

288

$$\zeta = \frac{\tau_m(u)}{\tau(u, \theta)} \leq 1 \tag{32}$$

289

290 where τ_m and $\tau(u, \theta)$ is respectively the mean and the maximum bond stress around the

291 circumference of a steel bar in an arbitrary cross section, and further multiplying χ in Eq. (30) by

292 ζ from Eq. (32) takes into account the bond stress τ not being constant around the

293 circumference of the steel bar in non-axisymmetric cases, e.g. when the cover to the steel

294 surface varies in a cross section as depicted in Fig. 2(d). In practice, this implies taking the

295 distance between rebars into account, a parameter acknowledged by the research of Gergely

296 and Lutz (1968) to be significant for the crack width. This means that the solution of Eq. (30)

297 with χ multiplied by ζ from Eq. (32) involves transforming a cross section with an arbitrary

298 geometry into a circular cross section with a radius r_{eq} such that the area A_c remains the same.

299

300 The analytical solution of Eq. (30) depends on the choice of the bond-slip law and a variety of

301 choices can be found in the literature (Rehm 1961, Nilson 1972, Martin 1973, Dörr 1978, Mirza

302   and Houde 1979, Hong and Park 2012). In this study, the local bond-slip law recommended by

303   MC2010 was used:

304

$$\tau(u) = \tau_{\max}\left(\frac{u}{u_1}\right)^\alpha \tag{33}$$

305

306   Eq. (33) and its parameters were originally derived on the basis of pull-out tests of relatively

307   short specimens, in which the concrete was in compression, thus differing considerably from the

308   stress conditions in RC ties where the concrete is in tension (Pedziwiatr 2008). However, the

309   investigation by Tan et al. (2018c) showed that Eq. (33) could be applied to represent the mean

310   bond transfer over the specimen length by using the predefined parameters $\tau_{\max} = 5.0$ MPa,

311    $u_1 = 0.1$ and $\alpha = 0.35$ when comparing it to the local bond-slip curves obtained from the FE

312   analysis of several RC ties, see Fig. 4. Bond-slip curves proposed by other authors are also

313   shown in the same figure. This means that inserting Eq. (33) in Eq. (30) finally yields the SODE

314

$$\frac{d^2u}{dx^2} - \chi\frac{\tau_{\max}}{u_1^\alpha}u^\alpha = 0 \tag{34}$$

315

316   Note that Eq. (34) has been derived and will be solved using the simplified equations for

317   concrete.

318

319   **4. The analytical crack width calculation model**

320   ***4.1 General solutions***

321   *4.1.1 The slip*

322   Eq. (34) is a non-linear homogenous SODE and can be solved analytically, by successively

323   defining the second term as a function of the slip $f(u)$, moving it to the other side of the equal

324   sign, multiplying both sides with the first derivative of the slip u', applying the chain rule on the

325   left-hand side of the equal sign and the substitution rule on the right-hand side, and

326   subsequently integrating once, the first derivative of the slip is provided as

327

$$u' = \frac{du}{dx} = -\sqrt{2(\gamma u^\beta + C)} \tag{35}$$

328

329   where C is an integration constant and

330

$$\beta = 1 + \alpha \tag{36}$$

331   and

$$\gamma = \chi \frac{\tau_{\max}}{\beta u_1^\alpha} \tag{37}$$

332

333   Only the negative sign is included in Eq. (35) for compatibility with Eq. (25). Separating the

334   variables in Eq. (35) and integrating on both sides yields

335

$$x = B - \frac{1}{\sqrt{2}} \int (\gamma u^\beta + C)^{-\frac{1}{2}} du \tag{38}$$

336

337   where B is an integration constant. The integral can now be solved using the method proposed

338   by Russo et al. (1990) and Russo and Romano (1992), where the binomial in Eq. (38) is

339   developed as an infinite series of functions in accordance with Newton's binomial theorem, and

340   then integrating each term. This results in two different general solutions that converge at

341   distinct intervals

342

$$x = B_1 - \frac{1}{\sqrt{2}} \sum_{k=0}^{\infty} \binom{-\frac{1}{2}}{k} \gamma^k \left(\frac{1}{C}\right)^{\left(\frac{1}{2}+k\right)} \frac{u^{1+k\beta}}{1+k\beta} \quad \text{for } 0 < u < u_{\mathrm{d}} \tag{39}$$

343

344   and

345

$$x = B_2 - \frac{1}{\sqrt{2\gamma}} \sum_{k=0}^{\infty} \binom{-\frac{1}{2}}{k} \left(\frac{C}{\gamma}\right)^k \frac{u^{\delta-k\beta}}{\delta-k\beta} \quad \text{for } u > u_{\mathrm{d}} \tag{40}$$

346

347   where B_1 and B_2 are integration constants, and

348

$$\delta = \frac{1 - \alpha}{2} \tag{41}$$

349

350   while

351

$$u_\mathrm{d} = \left|\frac{C}{\gamma}\right|^{\frac{1}{\beta}} \tag{42}$$

352

353   is the value discerning Eq. (39) from (40). Note that the general solutions in Eq. (39) and (40)

354   imply that the longitudinal coordinate x is a function of the slip value u as a consequence of

355   splitting the variables in Eq. (35).

356

357   *4.1.2 Strains*

358   Successively inserting Eq. (2) and (19) in Eq. (26), integrating once, and applying $\varepsilon_\mathrm{ci} = 0$ and

359    $\varepsilon_\mathrm{s} = F/E_\mathrm{s}A_\mathrm{s} = \varepsilon_\mathrm{s0}$ at the loaded end, i.e. at $x = 0$, yields

360

$$\varepsilon_\mathrm{ci} = \xi(\varepsilon_\mathrm{s0} - \varepsilon_\mathrm{s}) \tag{43}$$

361

362   Inserting Eq. (35) and (43) in Eq. (25) yields the steel strains

363

$$\varepsilon_\mathrm{s} = \frac{\xi\varepsilon_\mathrm{s0} + \sqrt{2(\gamma u^\beta + C)}}{1 + \xi} \tag{44}$$

364

365   while, inserting Eq. (44) in (43) provides the concrete strains

366

$$\varepsilon_\mathrm{ci} = \xi\frac{\varepsilon_\mathrm{s0} - \sqrt{2(\gamma u^\beta + C)}}{1 + \xi} \tag{45}$$

367

368   **4.2 Boundary conditions**

369   Boundary conditions must be established before calculating particular solutions. These are

370   established by considering the concepts of *comparatively lightly loaded members* (CLLM) and

371   *comparatively heavily loaded members* (CHLM) depicted in Fig. 5. Russo and Romano (1992)

372   were the first to introduce these concepts, which were later acknowledged by *fib* bulletin 10

373   (2000). Briefly summarized, the main difference is that steel and concrete strains become

374   compatible, $\varepsilon_s = \varepsilon_{ci}$, at a certain distance x_r from the loaded end in the case of CLLM, while the

375   strains remain incompatible, $\varepsilon_s \neq \varepsilon_{ci}$, over the entire bar length in the case of CHLM. This further

376   implies, in accordance with Eq. (24), that the slip becomes zero at distance x_r from the loaded

377   end in the case of CLLM and at the symmetry section x_S in the case of CHLM. This yields the

378   following boundary conditions in the case of CLLM behavior:

379

$$-u_r = 0 \tag{46}$$

$$-u_r' = \varepsilon_s - \varepsilon_{ci} = 0$$

380

381   at $x = x_r$, and in the case of CHLM behavior:

382

$$-u_S = 0 \tag{47}$$

$$-u_S' = \varepsilon_s - \varepsilon_{ci} > 0$$

383

384   at $x = x_S = \frac{L}{2}$.

385

386   ***4.3 Comparatively lightly loaded members (CLLM)***

387   Applying the boundary conditions in Eq. (46) for Eq. (35) yields

388

$$C = 0 \tag{48}$$

389

390   Inserting Eq. (48) in (38), integrating once and applying the boundary conditions in Eq. (46)

391   again yields the expression for the slip in the case of CLLM behavior

392

$$u = \left[\delta\sqrt{2\gamma}(x_r - x)\right]^{\frac{1}{\delta}} \tag{49}$$

393

394 Inserting Eq. (48) in (44) and acknowledging that $\varepsilon_s = \varepsilon_{s0}$ at $x = 0$, provides the maximum slip at

395 the loaded end as

396

$$u_0 = \left(\frac{\varepsilon_{s0}^2}{2\gamma}\right)^{\frac{1}{\beta}} \tag{50}$$

397

398 Furthermore, inserting Eq. (50) in (49) for $x = 0$ yields the transfer length as

399

$$x_r = \frac{1}{\delta}\left[\varepsilon_{s0}\left(\frac{1}{2\gamma}\right)^{\frac{1}{2\delta}}\right]^{\frac{2\delta}{\beta}} \tag{51}$$

400

401 Note that the transfer length increases with increasing steel strains $\varepsilon_{s0} = F/E_sA_s$ at the loaded

402 end. Expressions for the steel and concrete strains can be finally obtained by inserting Eq. (49)

403 in respectively Eq. (44) and (45)

404

$$\varepsilon_s = \frac{\xi\varepsilon_{s0} + (2\gamma)^{\frac{1}{2\delta}}[\delta(x_r - x)]^{\frac{\beta}{2\delta}}}{1 + \xi} \tag{52}$$

405

$$\varepsilon_{ci} = \xi\frac{\varepsilon_{s0} - (2\gamma)^{\frac{1}{2\delta}}[\delta(x_r - x)]^{\frac{\beta}{2\delta}}}{1 + \xi} \tag{53}$$

406

407 One application of the particular solutions obtained could be in the case of two consecutive

408 cracks formed with a considerable distance between them. This means that a certain region,

409 $2(x_s - x_r)$, remains undisturbed as depicted in Fig. 5(a) and (b). This situation occurs typically in

410 the so-called *crack formation stage*, in which the applied member load is relatively low and the

411 distance between two consecutive cracks formed is relatively large.

412

413 **_4.4 Comparatively heavily loaded members (CHLM)_**

414 _4.4.1 Particular solutions_

415 Applying the boundary conditions in Eq. (47) in (35) yields

416

$$u'_s = -\sqrt{2C} \tag{54}$$

417

418 Acknowledging from Eq. (35) and Fig. 5 that u' is a real function yields

419

$$C > 0 \tag{55}$$

420

421 This means that the general solutions of Eq. (39) and (40) apply in the case of CHLM because

422 $C \neq 0$. Now, inserting Eq. (35) in (25) and applying $\varepsilon_{ci} = 0$ and $\varepsilon_s = F/E_s A_s = \varepsilon_{s0}$ at the loaded

423 end, i.e. at $x = 0$, yields

424

$$C = \frac{\varepsilon_{s0}^2}{2} - \gamma u_0^\beta \tag{56}$$

425

426 Furthermore, Eq. (55) and (56) imply that the maximum slip at the loaded end must satisfy

427

$$u_{0,\max} = \left(\frac{\varepsilon_{s0}^2}{2\gamma}\right)^{\frac{1}{\beta}} \tag{57}$$

428

429 Inserting Eq. (56) in (42) and acknowledging that Eq. (37) is a positive value provides

430

$$u_d = \left(\frac{\varepsilon_{s0}^2}{2\gamma} - u_0^\beta\right)^{\frac{1}{\beta}} \tag{58}$$

431

432 Now, applying the first condition in Eq. (47) to (39) yields

433

$$B_1 = \frac{L}{2} \tag{59}$$

434

435   Moreover, applying $u = u_0$ at $x = 0$ for Eq. (40) yields that B_2 can be expressed with binomial

436   coefficients as

437

$$B_2 = \frac{1}{\sqrt{2\gamma}} \sum_{k=0}^{\infty} \binom{-\frac{1}{2}}{k} \left(\frac{C}{\gamma}\right)^k \frac{u_0^{\delta - k\beta}}{\delta - k\beta} \tag{60}$$

438

439   The particular solutions of Eq. (39) and (40) are now obtained using the integration constants in

440   Eq. (56), (59) and (60). It should be noted, however, that the integration constants in Eq. (56)

441   and (60) depend on the slip at the loaded end u_0, so they must be obtained iteratively. This can

442   be done conveniently by considering the two cases shown in Fig. 6.

443

444   *4.4.2 Case 1*

445   The first case involves solving Eq. (39) with respect to the slip at the loaded end in its interval

446   when $u_0 < u_\mathrm{d}$ in accordance with Fig. 6(a). Inserting Eq. (59) in (39) and applying $u = u_0$ at $x =$

447   0 provides the function

448

$$f_1(u_0) = \frac{L}{2} - \frac{1}{\sqrt{2}} \sum_{k=0}^{\infty} \binom{-\frac{1}{2}}{k} \gamma^k \left(\frac{1}{C}\right)^{\left(\frac{1}{2}+k\right)} \frac{u_0^{1+\beta k}}{1+\beta k} = 0 \tag{61}$$

449

450   which is valid for the interval

451

$$0 \le u_0 < \left(\frac{\varepsilon_{s0}^2}{4\gamma}\right)^{\frac{1}{\beta}} \tag{62}$$

452

453   when acknowledging that u_d in Eq. (39) is given by Eq. (58).

454

455   *4.4.3 Case 2*

456   Case 2 is where $u_0 > u_d$, which means that the solution for the slip u depends on both Eq. (39)

457   and (40) due to the validity of the equations at its respective intervals, see Fig. 6(b). In other

458   words, Eq. (39) is valid for slip values below u_d while Eq. (40) is valid for slip values above u_d.

459   Now, accepting that Eq. (39) is valid for the slip value $u = u_\mathrm{d} - du$ at the location $x_\mathrm{d} + dx_1$

460   provides

461

$$x_\mathrm{d} + dx_1 = \frac{L}{2} - \frac{1}{\sqrt{2}} \sum_{k=0}^{\infty} \binom{-\frac{1}{2}}{k} \gamma^k \left(\frac{1}{C}\right)^{\left(\frac{1}{2}+k\right)} \frac{(u_\mathrm{d} - du)^{1+\beta k}}{1+\beta k} \tag{63}$$

462

463   Similarly, accepting that Eq. (40) is valid for the slip value $u = u_\mathrm{d} + du$ at the location $x_\mathrm{d} - dx_2$

464   and inserting Eq. (60) provides

465

$$x_\mathrm{d} - dx_2 = \frac{1}{\sqrt{2\gamma}} \sum_{k=0}^{\infty} \binom{-\frac{1}{2}}{k} \left(\frac{C}{\gamma}\right)^k \frac{u_0^{\delta-k\beta}}{\delta - k\beta}$$

$$- \frac{1}{\sqrt{2\gamma}} \sum_{k=0}^{\infty} \binom{-\frac{1}{2}}{k} \left(\frac{C}{\gamma}\right)^k \frac{(u_\mathrm{d} + du)^{\delta-k\beta}}{\delta - k\beta} \tag{64}$$

466

467   Note that du is an infinitesimal value for the slip, while dx_1 and dx_2 are infinitesimal values

468   along the bar length in accordance with Fig. 6(b). Subtracting Eq. (64) from (63) provides the

469   function

470

$$f_2(u_0) = \frac{L}{2} - \frac{1}{\sqrt{2\gamma}} \{f_{21}(u_0) - f_{22}(u_0)\} - \frac{1}{\sqrt{2}} f_{23}(u_0) - \Delta x = 0 \tag{65}$$

471

472   where

473

$$f_{21}(u_0) = \sum_{k=0}^{\infty} \binom{-\frac{1}{2}}{k} \left(\frac{C}{\gamma}\right)^k \frac{u_0^{\delta-k\beta}}{\delta - k\beta} \tag{66}$$

474

$$f_{22}(u_0) = \sum_{k=0}^{\infty} \binom{-\frac{1}{2}}{k} \frac{\left[\left(\frac{C}{\gamma}\right)^{\frac{k}{\delta-k\beta}+\frac{1}{\beta}} + du\left(\frac{C}{\gamma}\right)^{\frac{k}{\delta-k\beta}}\right]^{\delta-k\beta}}{\delta - k\beta} \tag{67}$$

475

$$f_{23}(u_0) = \sum_{k=0}^{\infty} \binom{-\frac{1}{2}}{k} \frac{\gamma^k \left[C^{\frac{2-\beta}{2\beta(1+k\beta)}}\left(\frac{1}{\gamma}\right)^{\frac{1}{\beta}} - duC^{\frac{\frac{1}{2}+k}{1+k\beta}}\right]^{1+k\beta}}{1 + k\beta} \tag{68}$$

476

477 and $\Delta x = dx_1 + dx_2$. Eq. (65) is valid for

478

$$u_0 > \left(\frac{\varepsilon_{s0}^2}{4\gamma}\right)^{\frac{1}{\beta}} \tag{69}$$

479

480 when acknowledging that u_d in Eq. (40) is given by Eq. (58).

481

482 *4.4.4 Solution strategy*

483 Russo and Romano (1992) give a convenient way of determining whether Case 1 or Case 2

484 governs by calculating Eq. (61) for a value of u_0 close to the upper limit value in Eq. (62), e.g. as

485 $u_{0\text{check}} = \left(\frac{\varepsilon_{s0}^2}{4\gamma} - du\right)^{\frac{1}{\beta}}$. Case 1 governs if the value calculated is negative. Case 2 governs if the

486 value calculated is positive since the nature of Eq. (61) invokes that u_0 must increase to satisfy

487 Eq. (61), which implies that Eq. (69) governs.

488

489 Newton-Raphson iterations are used to calculate the value of u_0 effectively after determining

490 whether Case 1 or 2 governs

491

$$u_{0,i+1} = u_{0,i} - \frac{f_j(u_{0,i})}{f_j{}'(u_{0,i})} \tag{70}$$

492

493 where index i represents the number of iterations and index j represents the function in Eq. (61)

494 for Case 1 or Eq. (65) for Case 2. Furthermore, it is suggested that an initial value of $u_{0,\text{init}} =$

495 $\left(\frac{\varepsilon_{s0}^2}{4\gamma}\right)^{\frac{1}{\beta}} - du$ is used for Case 1 or $u_{0,\text{init}} = \left(\frac{\varepsilon_{s0}^2}{4\gamma}\right)^{\frac{1}{\beta}} + du$ is used for Case 2 to start the iterations in

496 Eq. (70). The iterated value $u_{0,i+1}$, however, should never exceed Eq. (57) due to the

497 requirement of Eq. (55). Convergence is achieved when $\left|u_{0,i+1} - u_{0,i}\right| < Tol$, at which Tol is a

498 chosen tolerance value. Note that the derivatives of the functions in Eq. (61) and (65) are

499 needed to solve Eq. (70) and are provided in Appendix A. Once the value of u_0 is obtained, the

500 particular solutions of Eq. (39) and (40) are used to obtain the corresponding x values for the

501 slip u along the bar length. In summary, CHLM involves determining whether Case 1 or 2

502 governs using Eq. (61) before the slip at the loaded end u_0 is calculated using Eq. (70).

503

504 *4.4.5 Strains*

505 The strain distributions for steel and concrete were obtained by using Eq. (44) and (45)

506 respectively. Moreover, inserting Eq. (45) in (15), and acknowledging that the maximum

507 concrete strains will occur at the symmetry section, i.e. where the slip $u = 0$, provides the

508 maximum mean concrete strains as

509

$$\varepsilon_{\text{cm,max}} = \psi\xi\frac{\varepsilon_{s0} - \sqrt{2C}}{1 + \xi} < \varepsilon_{\text{ct}} \tag{71}$$

510

511 The violation of Eq. (71) implies that a crack has formed at the symmetry section, meaning a

512 new member with length $L/2$ exists and that the CHLM response should be determined for the

513 newly formed member.

514

515 **4.5 Conditions at crack formation**

516 The conditions at crack formation are shown in Fig. 7, where the transfer length increases with

517 increasing load as highlighted for Eq. (51). The steel strain at the loaded end needed to extend

518 the transfer length to the symmetry section is obtained by inserting $x_{\text{r}} = L/2$ in Eq. (51) so that

519

$$\varepsilon_{s0,S} = (2\gamma)^{\frac{1}{2\delta}} \left(\frac{L}{2}\delta\right)^{\frac{\beta}{2\delta}}$$

(72)

520

521   Furthermore, the maximum mean concrete strain at the end of the transfer length x_r is obtained

522   by inserting Eq. (53) in (15) at $x = x_r$ so that

523

$$\varepsilon_{cm,max} = \frac{\psi\xi}{1+\xi}\varepsilon_{s0}$$

(73)

524

525   It is assumed that a crack forms when $\varepsilon_{cm,max} = \varepsilon_{ct}$, which means that the corresponding steel

526   strain at the loaded end is

527

$$\varepsilon_{s0,cr} = \varepsilon_{ct}\frac{1+\xi}{\psi\xi}$$

(74)

528

529   So inserting Eq. (74) in (51) yields the distance from the loaded end at which a new crack can

530   form or, expressed more rigorously, the *crack spacing*

531

$$x_{cr} = \frac{1}{\delta}\left[\varepsilon_{ct}\frac{1+\xi}{\psi\xi}\left(\frac{1}{2\gamma}\right)^{\frac{1}{2\delta}}\right]^{\frac{2\delta}{\beta}}$$

(75)

532

533   Eq. (72) to (75) are conceptually visualized in Fig. 7, providing two different conditions for the

534   cracking response of a member. The continuous lines represent the steel strains, while the

535   dashed lines represent the corresponding concrete strains. Note that the concrete strain for $\varepsilon_{s0,S}$

536   in Fig. 7(a) is unrealistic since the concrete tensile strength is exceeded. It is only included to

537   elucidate the physical concept of Eq. (72). Condition 1 implies that a crack forms at a distance

538   from the loaded end shorter than half the member length, i.e. $x_{cr} < x_S$, meaning that $\varepsilon_{s0,cr} <$

539    $\varepsilon_{s0,S}$. This further implies that the cracking response of the member is governed by CLLM

540   behavior as long $\varepsilon_{s0} < \varepsilon_{s0,cr}$, while CHLM behavior governs the cracking response as soon as

541    $\varepsilon_{s0} > \varepsilon_{s0,cr}$. Condition 2 implies that a crack can form only at the symmetry section, $x_{cr} = x_s$,

542 because $\varepsilon_{s0,cr} > \varepsilon_{s0,S}$. This means that a CLLM behavior governs the cracking response of the

543 member as long $\varepsilon_{s0} < \varepsilon_{s0,S}$, while CHLM behaviour governs the cracking response as soon

544 $\varepsilon_{s0} > \varepsilon_{s0,S}$. The physical interpretation of Condition 1 is that cracking can form at any location

545 beyond x_r due to the unrestricted length of the member, while Condition 2 means that cracking

546 can form only at the symmetry section due to the limited length of the member. Appendix B

547 provides guidelines for determining which condition applies and whether CLLM or CHLM

548 behavior governs the cracking response based on the a priori loading and the mechanical

549 properties of the RC tie. For design purposes, however, only Condition 1 is relevant for

550 determining the cracking response.

551

552 **4.6 The crack width**

553 Finally, the crack width is obtained as

554

$$w_{cr} = 2 \int_{x_r} (\varepsilon_s - \varepsilon_{cm}) dx \tag{76}$$

555

556 Inserting Eq. (15), (44) and (45) in Eq. (76) yields

557

$$w_{cr} = 2 \left(\frac{1}{1 + \xi} \right) [\xi \varepsilon_{s0} x_r (1 - \psi) + u_0 (1 + \psi \xi)] \tag{77}$$

558

559 In summary, the crack width is a function of the applied load $\varepsilon_{s0} = F/A_s E_s$, the transfer length x_r,

560 and the slip at the loaded end u_0. For design purposes, i.e. Condition 1, the crack width is

561 determined by calculating u_0 and x_r, which in the case of CLLM behavior is obtained by the

562 closed-form solutions in Eq. (50) and (51). A solution strategy is provided in subsection 4.4.4 to

563 calculate u_0 efficiently in the case of CHLM behavior, but here x_r is replaced with $\frac{x_{cr}}{2}$, where x_{cr}

564 is the crack spacing obtained using the closed-form solution in Eq. (75). Note that the crack

565 width obtained w_{cr} applies to the face at the loaded rebar end, i.e. as depicted in Fig. 1. This

566 means that the calculation model conservatively assumes that a crack has been formed before

567 loading, which allows for predicting crack widths regardless of the load level.

568

4.7 Comparison with equivalent calculation models

570   The calculation model described was evaluated against the equivalent models proposed by

571   Russo and Romano (1992), Balász (1993) and Debernardi and Taliano (2016). The models are

572   equivalent in the sense that the SODE for the slip, i.e. Eq. (34), is solved. However, some

573   significant differences should be highlighted. The models of Balász (1993) and Debernardi and

574   Taliano (2016) neglect the elastic shear deformation over the cover, i.e. they assume $\psi = 1$ in

575   Eq. (14). Another significant difference in Debernardi and Taliano (2016) is that the bond stress

576   distribution over the bar length is altered locally by using a linear descending branch close to the

577   primary crack, which complicates the solution of Eq. (34). These authors assume that internal

578   inclined cracks form in this region and continue to form towards the symmetry section as the

579   load increases. The FE analysis by Lutz (1970) and by Tan et al. (2018c) on RC ties show that

580   a build-up of bond stresses occurs close to a primary crack and that the peak of the bond stress

581   distribution tends to move towards the symmetry section as the load increases, as assumed by

582   Debernardi and Taliano (2016). However, this physical phenomenon is a consequence not of

583   internal inclined cracks, but of internal splitting cracks forming close to the primary crack, which

584   is reflected by the characteristic bond-slip curves at $x \approx 0$ in Fig. 4. In fact, the FE analysis

585   showed that internal inclined cracks also formed beyond the bond stress distribution peak,

586   which means they cannot occur in direct conjunction with the descending branch alone. This

587   also means that a single bond-slip curve should suffice to represent the mean local bond-slip

588   behavior over the bar length, as shown in Fig. 4 and discussed in Section 2, and should already

589   include the total effect of both internal splitting and internal inclined cracks have on reducing the

590   bond transfer.

591

592   The calculation model presented in this paper was particularly inspired by the work of Russo

593   and Romano (1992). However, there are some significant differences: (i) a primary crack is

594   assumed to form when, $\varepsilon_{cm} = \varepsilon_{ct}$, implying that concrete stresses are unevenly distributed even

595   at the zero-slip section in accordance with the observations in Fantilli et al. (2008) and Tan et al.

596   (2018b); (ii) the influence of the distance between steel bars can be accounted for by Eq. (32);

597   and (iii) a completely analytical solution strategy is provided to solve Eq. (34) for practical

598   applications. In addition, the derivations using continuum mechanics formulation yield a

599   mechanically sound model that describes how the 3D behavior of RC ties can be simplified into

600   a 1D model when using a proper bond-slip law. However, the main advantage of the model

601   presented in this paper, and that of Russo and Romano (1992), is that Eq. (34) is solved

602   completely analytically, in contrast to Balász (1993) and Debernardi and Taliano (2016), who

603   only provide analytical solutions in the case of CLLM behavior.

604

605   Using the bond-slip curve recommended by Tan et al. (2018c) implies that the bond stresses

606   should be related to the deformations in the outer surface of the concrete rather than at the

607   steel-concrete interface, which contradicts the compatibility in Eq. (24). However, the elastic

608   shear deformation over the cover is normally considered to be negligible, although it does seem

609   to affect the elastic stress and strain distribution (Braam 1990, Tan et al. 2018b). This justifies

610   the combined use of the chosen bond-slip curve, the compatibility in Eq. (24), and the concept

611   of ψ in Eq. (14).

612

613   **5. Application**

614   ***5.1 Comparison with axisymmetric RC ties***

615   *5.1.1 General*

616   This section compares strains and crack widths obtained analytically with the classical

617   experiments of Bresler and Bertero (1968) and Yannopoulos (1989), and the FE analysis of Tan

618   et al. (2018c) on cylindrical RC ties concentrically reinforced with a steel bar loaded at the steel

619   bar ends. The bond-slip parameters, $\tau_{max} = 5.0 \text{ MPa}$, $u_1 = 0.1 \text{ mm}$ and $\alpha = 0.35$ were chosen,

620   while $\psi = 0.70$ was adopted in accordance with Tan et al. (2018b). The factor $\zeta = 1$ was chosen

621   due to axisymmetry. The infinite series used for calculating the response in the case of CHLM

622   behavior was truncated after 10 terms, while the parameters $\Delta x = 0.1$ and $du = 5.8 \cdot 10^{-5}$ were

623   chosen in accordance with Russo and Romano (1992).

624

625   *5.1.2 Comparison with experimental data*

626   Bresler and Bertero (1968) measured the strain distribution over the bar length by mounting

627   several strain gauges in a groove cut along the center of several reinforcing steel bars. The

628   reinforcing steel bars were first cut longitudinally into two halves, after which the groove was

629   milled along the center of the two parts. After mounting the strain gauges in this groove, the two

630   halves were tack-welded together to minimize the impact on the exterior of the reinforcing bars.

631   The specimen investigated, denoted "Specimen H", was 406.4 mm (16 in) long and 152.4 mm

632   (6 in) in diameter concentrically reinforced with a 28.7 mm (1.13 in) deformed steel bar. The

633   length of the specimen was chosen as twice the mean crack spacing of 203.2 mm (8 in)

634   obtained from pilot studies conducted on 1829 mm (72 in) long RC ties with similar sectional

635   properties. A notch was cut around the circumference at mid-length to induce cracking here.

636   The compressive strength, tensile strength, and Young's modulus for the concrete were

637   reported as respectively 40.8 MPa (5.92 ksi), 4.48 MPa (0.65 ksi), and 33165 MPa (4810 ksi),

638   while the yield strength and Young's modulus for the steel were reported as 413 MPa (60 ksi)

639   and 205464 MPa (29800 ksi) respectively. The reduction of the steel area due to the groove was

640   taken into account in the analytical calculations by using the reported steel area $A_s =$

641   548 mm^2 (0.85 in^2), while the notch was taken into account by reducing the reported tensile

642   strength by a factor of 0.7. This led to cracking at mid-length in the analytical calculations for

643   higher load levels as shown in Fig. 8(a). It should be noted that the analytical steel strains

644   represent the mean of the experimental steel strains.

645

646   The six specimens investigated by Yannopoulos (1989) were 76 mm in diameter concentrically

647   reinforced with a 16 mm deformed steel bar and were 100 mm long. The length of the

648   specimens was based on the mean crack spacing of 90 mm obtained from pilot studies

649   conducted on 800 mm long RC ties with similar sectional properties and was chosen to prevent

650   new cracks from forming between the loaded ends. The compressive strength, tensile strength,

651   and Young's modulus for concrete were reported respectively as 43.4 MPa, 3.30 MPa and

652   32000 MPa, while the yield strength and Young's modulus for steel were reported as 424 MPa

653   and 200000 MPa respectively. The specimen length in the analytical calculations was chosen to

654   be similar to that in the experiments. Fig. 8(b) shows the average crack width development at

655   the loaded ends reported for the six specimens investigated. The analytical calculations

656   predicted slightly larger crack widths. Nevertheless, the comparison shows good agreement.

657

658   *5.1.3 Comparison with FE analysis*

659   Tan et al. (2018c) conducted NLFEA on four cylindrical RC ties denoted $\phi20c40$, $\phi32c40$,

660     $\phi20c90$, and $\phi32c90$ using axisymmetric elements, with ϕ and c respectively indicating steel bar

661   diameter and cover. The concrete was given material properties corresponding to a concrete

662   grade C35 in accordance with MC2010 and a non-linear fracture mechanics material model

663   based on total strain formulation with rotating cracks. The crack bandwidth was chosen to be

664   dependent on the total area of the finite elements in line with the smeared crack approach. The

665   steel was chosen to have linear elastic material properties with a Young's modulus of

666   200000 MPa and a Poisson's ratio of 0.3. Furthermore, interface elements were used to allow

667   for radial separation but no physical slip, as depicted in Fig. 1(b). In summary, the approach

668   implied smearing out internal inclined and splitting cracks that would have localized at the tip of

669   each bar rib if they were modelled discretely. This was found to give good agreement in

670   comparison with the steel strains, development of crack widths, and mean crack spacing

671   observed in the experiments.

672

673   Fig. 9 shows the comparison of steel strain distributions over the bar lengths at three different

674   stress levels for the specimens, again noting that the analytical model predicts the mean of the

675   experimental steel strains. The first stress level shows the CLLM behavior just before a crack

676   forms at a certain distance from the loaded end, while the two higher stress levels show the

677   CHLM behavior for specimen lengths similar to the crack spacing obtained in the FE analysis,

678   see Table 1. Note that the strain distribution is shown for only half the specimen length due to

679   symmetry. In general, the analytical calculations make conservative predictions of the CLLM

680   behavior, which also is reflected in the comparison of the predicted crack spacing in Table 1.

681   The table also shows that the analytical model predicts crack spacing consistently and on the

682   conservative side regardless of the bar diameter and cover size. The conservative prediction of

683   the crack spacing can be attributed to the bond-slip parameters chosen. Fig. 10 shows the

684   development of crack widths in specimens with lengths similar to the FE analysis crack spacing

685   in Table 1 and indicates that the analytical model makes quite accurate predictions of crack

686   widths for a given specimen length.

687

688   Fig. 11 shows comparisons of the development of crack widths based on specimen lengths

689   similar to the crack spacing predicted by the analytical model in Table 1. The analytical model

690   yields Condition 2 and CHLM behavior in general, which allows for cracking at mid-length at

691   higher load levels and occurs for all of the specimens except $\phi 20 c 90$. The graphs also show

692   that the analytical model predicts crack widths on the conservative side in general.

693

694   ***5.2 Comparison with non-axisymmetric RC ties***

695   The French research project CEOS.fr (2016) conducted experiments on two identical quadratic

696   RC ties identified as Ties 4 and 5 which were pulled in tension. The ties were 355 mm in width

697   and height, had a length of 3200 mm, and were reinforced with eight 16 mm rebars. A concrete

698   grade C40/50 was used, while the yield strength and Young's modulus of steel were reported as

699   529 MPa and 200000 MPa respectively. The cover to the rebars was 45 mm. Fig. 12(a) shows a

700   comparison of the development of predicted crack widths with the maximum crack widths

701   measured. The analytical calculations were based on using specimen lengths similar to the

702   crack spacing predicted analytically in Table 2. The factor $\zeta = 1$ was chosen for simplicity. The

703   deviation between Tie 4 and Tie 5 in the maximum crack widths measured seems to be due to

704   the difference in maximum crack spacing reported in Table 2. Nevertheless, the maximum crack

705   spacing predictions were conservative, and the crack widths predicted show relatively good

706   agreement with the maximum crack widths measured.

707

708   Tan et al. (2018a) conducted experiments on eight quadratic RC ties identified as X-ϕ-c, where

709   X represents the loading regime the RC tie was exposed to, either at the crack formation stage

710   (F) or the stabilized cracking stage (S), while ϕ and c represent the rebar diameter and cover

711   respectively. The rebar diameter was either 20 mm or 32 mm, while the cover was either 40 mm

712   or 90 mm. The ties were 400 mm in width and height, had a length of 3000 mm, and were

713   reinforced with eight rebars. The concrete compressive and tensile strength were reported as

714   74.3 MPa and 4.14 MPa respectively, while the Young's modulus was reported as 27.4 MPa.

715   The yield strength and Young's modulus of the steel were reported as 500 MPa and 200000

716   MPa respectively. Fig. 12(b) shows the comparison of maximum crack widths measured $w_{0.95}$

717   and crack widths predicted w_{cr} using the concept of modelling uncertainty, i.e. as $\theta = w_{0.95}/w_{\mathrm{cr}}$.

718   The crack widths calculated were based on using specimen lengths similar to the crack spacing

719   predicted analytically in Table 2. The factor $\zeta = 1$ was again chosen for simplicity. Both the

720   crack widths and the crack spacing predicted are on the conservative side except for F-32-90

721   and S-32-90, in which the maximum crack widths predicted were slightly underestimated.

722

723   **6. Discussion**

724   The conservative predictions of the crack widths in Fig. 11 are due to the nature of Eq. (75),

725   which, together with the predefined bond-slip parameters, provides an upper limit for the crack

726   spacing or, expressed more rigorously, for the maximum crack spacing. This is equivalent to the

727   concept of calculating the maximum crack widths according to the semi-empirical formulas in

728   EC2 and MC2010. However, unlike EC2 and MC2010, Eq. (75) is not assumed to vary from

729   once to twice this value. Furthermore, Figs. 8b) and 10 show the ability of the model to predict

730   accurate crack widths given a specimen length. The observations in Figs. 8a) and 9 suggest

731   that the analytical model can predict the mean behavior of experimental steel strains, which is a

732   direct result of using just one local bond-slip curve to represent the bond transfer over the

733   specimen length. This means that the effect internal inclined and splitting cracks has on

734   reducing the bond transfer locally is smeared over the specimen length in the analytical model.

735   The consequence of using only one local bond-slip curve is that the bond stresses reach their

736   maximum at the cracked section ($x = 0$), which contradicts the physical behavior of RC ties

737   discussed previously. This is due to the fact that the selected bond-slip curve causes bond

738   stresses to increase with increasing slip as can be observed in Fig. 4. This is elucidated in Fig.

739   13, which shows the corresponding bond stresses to the steel strains predicted in Fig. 9. One

740   solution to this problem would be to use different bond-slip curves depending on the location

741   over the specimen length, but this would substantially complicate the solutions to the analytical

742   model. So, the use of just one local bond-slip curve provides a practical yet mechanically sound

743   calculation model that has proven capable of predicting the development of crack widths and

744   crack spacing consistently and on the conservative side, regardless of the mechanical

745   properties and loading of the RC ties. Another advantage of using a bond-slip curve, as

746   opposed to assuming a constant bond stress distribution e.g. in EC2 and MC2010, is that the

747   mean bond stresses become dependent on the load level and the geometry of RC tie, thus

748   conforming to the theoretical observations made by Tan et al. (2018c). This should provide

749   more realistic predictions of the crack spacing.

750

751   Fig. 14 shows the corresponding concrete strains at the interface, ε_{ci}, to the steel strains

752   predicted in Fig. 9 at load levels 250 MPa and 400 MPa, whereas the dashed lines represent

753   the resultant of concrete strains in a section according to Eq. (15), i.e. as $\varepsilon_{cm} = \psi\varepsilon_{ci}$. It is

754   observed that both the concrete stresses at the interface and the resultants of concrete stresses

755   increase with increasing load level. This is due to the increase of the bond transfer between the

756   load levels of 250 MPa and 400 MPa as represented by the increase of the areas under the

757   curves shown in Fig. 13. Furthermore, this would cause a crack to form at the zero-slip section

758   even in the case of CHLM behavior if the mean concrete strains exceed the tensile strength of

759   concrete, as shown in Fig. 11. This conforms to the discussions of transient cracking of RC ties

760   addressed in *fib* bulletin No. 10 (*fib* 2000). This feature though, can easily be neglected in the

761   calculation model for design situations as a conservative approach. The main reason for

762   including ψ in Eq. (14) was to account for the fact that nonlinear strain profiles occur over the

763   concrete cover (Tan 2018b), which is a mechanical improvement to the assumption of claiming

764   that plane sections remain plane in RC ties as per (Saliger 1936, Balász 1993, CEN 2004, *fib*

765   2013 and Debernadi and Taliano 2016). It can be shown though, that different values of ψ in

766   general have limited effect on the crack width predictions.

767

768   Fig. 12 shows that the analytical model presented can be applied to predict crack widths in non-

769   axisymmetric RC ties as well. In these calculations, simple assumptions were made such as

770   that the whole concrete area contributed in tension $A_{c,ef} = A_c$ and choosing $\zeta = 1$. This led to

771   similar crack spacing predictions for RC ties with similar reinforcement ratios but different

772   covers, which contradicts the experimental data in Table 2. It is well-known that the cover has a

773   significant influence on crack spacing, and therefore crack widths, as reported by Broms (1968),

774   Gergely and Lutz (1968), Caldentey et al. (2013) and Tan et al. (2018a). One approach to taking

775   the cover into account could be to use the provisions in EC2 and MC2010 for calculating an

776   effective reinforcement ratio, $\rho_{s,ef} = A_s/A_{c,ef}$, to predict the cracking behavior.. This is

777   exemplified in Table 3, which shows the crack spacing predictions when the effective height

778 surrounding the rebars, i.e. $h_{c,ef} = \min[2.5(c + \phi/2), h/2]$, is used to determine the effective

779 reinforcement ratios. Comparison of specimens having similar geometrical reinforcement ratios,

780 e.g. S-20-40 against S-20-90 and S-32-40 against S-32-90, shows that the crack spacing

781 predictions increase for specimens having larger covers owing to the difference in effective

782 reinforcement ratios. However, the increase in crack spacing predictions for specimens with

783 larger covers is seen to be underestimated compared to the experimental evidence. This could

784 also be related to assuming $\zeta = 1$, which is questionable particularly for RC ties with 90 mm

785 cover because the bond stress distribution surrounding the perimeter of the rebars is probably

786 not uniform, as elucidated in Fig. 2(d). However, determining a proper value for ζ is not

787 straightforward and requires further study, e.g. by conducting FE analysis of non-axisymmetric

788 RC ties. Nevertheless, the model with the introduction of the factor ζ and an effective

789 reinforcement ratio based on the cover size shows great potential in predicting the cracking

790 behavior of non-axisymmetric RC ties as well.

791

792 The calculation model using the simplified equations for concrete can predict crack widths both

793 in the *crack formation stage* and the *stabilized cracking stage* through the concepts of CLLM

794 and CHLM, and is as such different from the calculation methods recommended by EC2 and

795 MC2010 which apply to the stabilized cracking stage only. Furthermore, assuming ψ not equal

796 to one implies that the mean concrete strains over the section in general is different from the

797 concrete strains at the interface further implying that the concrete stresses in each section are

798 assumed unevenly distributed, even at the zero-slip section, a concept first introduced by

799 Edwards and Picard (1972). This means that a crack forms when the resultant of concrete

800 stresses at the zero-slip section is equal to the mean value of the tensile strength as pointed out

801 for Eq. (74). Finally, using only one bond-slip curve means that bond stresses are different from

802 null at the cracked section. These assumptions enabled a practical approach to solve the SODE

803 for the slip.

804

805 The model allows for treating problems such as *imposed deformations,* where the mechanical

806 loading becomes directly dependent on the crack pattern or, expressed more rigorously, the

807 stiffness of the member. Moreover, the authors of this paper are also currently working on the

808   application of the analytical model to more general cases, such as non-cylindrical RC ties,

809   tensile zones in structural elements exposed to bending, and RC membrane elements exposed

810   to biaxial stress states at which cracks form at a skew angle to an orthogonal reinforcement

811   grid.

812

813   **7. Conclusions**

814   A new analytical crack width calculation model has been formulated to provide more consistent

815   crack width calculations for large-scale concrete structures, where large covers and bar

816   diameters are typically used. The calculation model was derived based on the uniaxial behavior

817   of axisymmetric RC ties. Furthermore, the model includes the effect of internal cracking on the

818   bond transfer, a non-uniform strain distribution over the concrete area and a non-uniform bond

819   stress distribution surrounding the perimeter of the steel bar in non-axisymmetric cases. The

820   latter accounts for the effect of steel bar spacing in practice.

821

822   The SODE for the slip has been solved completely analytically, yielding closed-form solutions in

823   the case of comparatively lightly loaded member (CLLM) behavior and non-closed-form

824   solutions in the case of comparatively heavily loaded member (CHLM) behavior. One solution

825   strategy and method for determining the complete cracking response has been provided for the

826   purposes of facilitating a practical applicable calculation model, the lack of which has been the

827   major drawback in using previous equivalent models. The comparison with experimental and

828   finite element results in the literature shows that the calculation model predicts an average

829   strain distribution based on using a single local bond-slip curve to represent the bond transfer.

830   The comparisons demonstrate the ability of the calculation model to predict crack widths

831   accurately given a member length. Finally, the model has proven capable of predicting crack

832   spacing and crack widths consistently and in general on the conservative side regardless of the

833   bar diameter and cover, even for non-axisymmetric RC ties.

834

33

839 **Appendix A**

840 Function derivatives in the case of CHLM behavior for Case 1.

841

$$f_1'(u_0) = -\frac{1}{\sqrt{2}} \sum_{k=0}^{\infty} \binom{-\frac{1}{2}}{k} \gamma^k \left[\gamma \beta u_0^{\beta-1} \left(\frac{1}{2}+k\right) C^{-\frac{3}{2}-k} \frac{u_0^{1+k\beta}}{1+k\beta} + C^{-\left(\frac{1}{2}+k\right)} u_0^{k\beta} \right] \tag{78}$$

842

843 Function derivatives in the case of CHLM behavior for Case 2.

844

$$f_2'(u_0) = -\frac{1}{\sqrt{2\gamma}} [f_{21}'(u_0) - f_{22}'(u_0)] - \frac{1}{\sqrt{2}} f_{23}'(u_0) \tag{79}$$

845

$$f_{21}'(u_0) = \sum_{k=0}^{\infty} \binom{-\frac{1}{2}}{k} \left(\frac{1}{\gamma}\right)^k \left[C^k u_0^{\delta-k\beta-1} - \frac{\gamma \beta k C^{k-1}}{\delta - k\beta} u_0^{\beta(1-k)+\delta-1} \right] \tag{80}$$

846

$$f_{22}'(u_0) = \sum_{k=0}^{\infty} \binom{-\frac{1}{2}}{k} \left[\left(\frac{C}{\gamma}\right)^{\frac{k}{\delta-k\beta}+\frac{1}{\beta}} + du \left(\frac{C}{\gamma}\right)^{\frac{k}{\delta-k\beta}} \right]^{\delta-k\beta-1} \cdot \left(-\gamma \beta u_0^{\beta-1}\right)$$

$$\cdot \left[\left(\frac{1}{\gamma}\right)^{\frac{k}{\delta-k\beta}+\frac{1}{\beta}} \left(\frac{k}{\delta-k\beta}+\frac{1}{\beta}\right) C^{\frac{k}{\delta-k\beta}+\frac{1}{\beta}-1} \right. \tag{81}$$

$$\left. + du \left(\frac{1}{\gamma}\right)^{\frac{k}{\delta-k\beta}} \left(\frac{k}{\delta-k\beta}\right) C^{\frac{k}{\delta-k\beta}-1} \right]$$

847

$$f_{23}'(u_0) = \sum_{k=0}^{\infty} \binom{-\frac{1}{2}}{k} \gamma^k \left[\left(\frac{1}{\gamma}\right)^{\frac{1}{\beta}} C^{\frac{2-\beta}{2\beta(1+k\beta)}} - du C^{-\frac{\frac{1}{2}+k}{1+k\beta}} \right]^{k\beta} \cdot \left(-\gamma \beta u_0^{\beta-1}\right)$$

$$\cdot \left\{ \left(\frac{1}{\gamma}\right)^{\frac{1}{\beta}} \left[\frac{2-\beta}{2\beta(1+k\beta)}\right] C^{\left[\frac{2-\beta}{2\beta(1+k\beta)}-1\right]} \right. \tag{82}$$

$$\left. + du \left[\frac{\frac{1}{2}+k}{1+k\beta}\right] C^{-\left[\frac{\frac{1}{2}+k}{1+k\beta}+1\right]} \right\}$$

848

849   **Appendix B**

850   A method for determining the complete cracking response, in which $\varepsilon_{s0,s}$, $\varepsilon_{s0,cr}$ and x_{cr} are

851   determined by Eq. (72), (74) and (75) respectively, while ε_{s0} is the steel strain at the loaded end.

852   CLLM and CHLM are abbreviations for *Comparatively Lightly Loaded Members* and

853   *Comparatively Heavily Loaded Members* respectively.

854

855

856 **References**

857 Balázs, G.L. (1993). "Cracking Analysis Based on Slip and Bond Stresses." *ACI Materials*

858   *Journal,* 90(4), 340-348.

859 Beeby, A.W. (2004). "The influence of the parameter ϕ/ρ_{eff} on crack widths." *fib Journal*

860   *Structural Concrete*, 5(2), 71-83.

861 Borosnyói, B., and Balázs, G.L. (2005). "Models for flexural cracking in concrete: the state of the

862   art" *fib Journal Structural Concrete,* 6(2), 53-62.

863 Borosnyói, A., and Snóbli, I. (2010). "Crack width variation within the concrete cover of

864   reinforced concrete members." *Építőanyag – Journal of Silicate Based and Composite*

865   *Materials*, 62(3), 70-74.

866 Bresler, B. and Bertero, V.V. (1968). "Behavior of reinforced concrete under repeated load."

867   *Proceedings of the ASCE – Journal of the Structural Division,* 94(6), 1567-1590.

868 Braam, C.R. (1990). "Control of crack width in deep reinforced concrete beams [PhD thesis]."

869   TU Delft, Delft, the Netherlands.

870 Broms, B. (1968). "Theory of the calculation of crack width and crack spacing in reinforced

871   concrete members." *Cement och Betong,* No. 1, 52-64.

872 Caldentey, A.P., Peiretti, H.C., Iribarren, J.P., and Soto, A.G. (2013). "Cracking of RC members

873   revisited: influence of cover, $\phi/\rho_{s,ef}$ and stirrup spacing – an experimental and theoretical

874   study." *fib Journal Structural Concrete,* 14(1), 69-78.

875 CEN. (2004). "EN 1992-1-1 Eurocode 2: Design of concrete structures – Part 1-1: General rules

876   and rules for buildings." European Committee for Standardization, Brussels, Belgium.

877 CEOS.fr. (2016). "Control of Cracking in Reinforced Concrete Structures." ISTE Ltd and John

878   Wiley & Sons, Inc, London and Hoboken, UK and USA.

879 Debernardi, P.G., and Taliano, M. (2016). "An improvement to Eurocode 2 and *fib* Model Code

880   2010 methods for calculating crack width in RC structures." *fib Journal Structural Concrete,*

881   17(3), 365-376.

882 Dörr, K. (1978). "Bond-Behaviour of Ribbed Reinforcement under Transversal Pressure. IASS

883   Symposium on Nonlinear Behaviour of Reinforced Concrete Spatial Structures." *Werner*

884   *Verlag*, Düsseldorf, Germany, Vol. 1, pp. 13-24.

885   Edwards, A.D., and Picard, A. (1972). "Theory of Cracking in Concrete Members." *Proceedings*

886   *of the ASCE – Journal of the Structural Division*, 98(12), 2687-2700.

887   Eligehausen. R., Popov. E.P., and Bertero. V.V. (1983). "Local bond stress-slip relationships of

888   deformed bars under generalized excitations: experimental results and analytical model."

889   Report No. UCB/EERC 83/23, University of California, Berkeley, USA.

890   Fantilli, A.P., Mihashi, H., and Vallini, P. (2007). "Crack profile in RC, R/FRCC and R/HPFRCC

891   members in tension." *Materials and Structures,* 40, 1099-1114.

892   *fib.* (2000). "Bond of reinforcement in concrete – State-of-the-art report." *fib bulletin No. 10*,

893   Lausanne, Switzerland.

894   *fib.* (2013). "*fib* Model Code for Concrete Structures 2010. International Federation for Structural

895   Concrete." Ernst & Sohn, Berlin.

896   Gergely, P., and Lutz, L.A. (1968). Maximum Crack Width in Reinforced Concrete Flexural

897   Members. Causes, Mechanisms and Control of Cracking in Concrete, SP-20, American

898   Concrete Institute, Farmington Hills, MI, USA, pp. 87-117.

899   Goto, Y. (1971) "Crack formed in concrete around deformed tension bars." *ACI Journal*, 68(4),

900   244-251.

901   Hong, S., and Park, S.K. (2012). "Uniaxial Bond Stress-Slip Relationship of Reinforcing Bars in

902   Concrete." *Advances in Materials Science and Engineering*. 2012 (2012), Article ID 328570.

903   Husain, S.I., and Ferguson, P.M. (1968). "Flexural crack width at the bars in reinforced concrete

904   beams. Research Report Number 102-1F." Center for Highway Research, The University of

905   Texas at Austin, USA.

906   Irgens, F. (2008). *Continuum Mechanics*, Springer, Bergen, Norway.

907   Kaklauskas, G. (2017). "Crack Model for RC Members Based on Compatibility of Stress-

908   Transfer and Mean-Strain Approaches." *J. Struct. Eng.,* 143(9). 10.1061/(ASCE)ST.1943-

909   541X.0001842.

910   Leonhardt, F. (1988). "Cracks and Crack Control in Concrete Structures." *PCI Journal,* Jul-Aug,

911   pp. 124-145.

912   Lutz, L.A. (1970) "Analysis of Stresses in Concrete Near a Reinforcing Bar Due to Bond and

913   Transverse Cracking." *ACI Journal,* 67(10): 778-787.

914 Martin, H. (1973). "On the interrelation among surface roughness, bond and bar stiffness in the

915   reinforcement subject to short-term loading (in German)." *Deutscher Ausschuss Stahlbeton,*

916   (228), 1-50.

917 Mirza, S.M., and Houde, J. (1979). "Study of Bond Stress-Slip Relationships in Reinforced

918   Concrete." *ACI Journal,* 76(1): 19-46.

919 Nilson, A.H. (1972). "Internal Measurement of Bond Slip." *ACI Journal,* 69(7), 439-441.

920 NPRA. (2015). "N400 Bruprosjektering: Prosjektering av bruer, ferjekaier og andre bærende

921   konstruksjoner." *N400* in *Statens vegvesens håndbokserie*, ISBN: 978-82-7207-680-0.

922 Pedziwiatr, J. (2008). "Influence of internal cracks on bond in cracked concrete structures."

923   *Archives of Civil and Mechanical Engineering*, 8(3), 91-105.

924 Rehm, G. (1961). "On the fundamentals of the steel-concrete bond (in German)." *Deutscher*

925   *Ausschuss für Stahlbeton*, (138), 1-59.

926 Russo, G., Zingone, G., and Romano, F. (1990). "Analytical Solution for Bond-Slip of

927   Reinforcing Bars in R.C. Joints." *J. Struct. Eng.,* 10.1061/(ASCE)0733-

928   9445(1990)116:2(336).

929 Russo, G., and Romano, F. (1992). "Cracking Response of RC Members Subjected to Uniaxial

930   Tension." *J. Struct. Eng.,* https://doi.org/10.1061/(ASCE)0733-9445(1992)118:5(1172).

931 Tan, R., Eileraas K., Opkvitne, O., et al. (2018a). "Experimental and theoretical investigation of

932   crack width calculation methods for RC ties." *fib Journal Structural Concrete, 1-12.*

933   https://doi.org/10.1002/suco.201700237.

934 Tan, R., Hendriks, M.A.N., and Kanstad, T. (2018b). "An investigation of the strain profile over

935   the cover in reinforced concrete elements subjected to tension." *fib Congress,* October 2018,

936   Melbourne, Australia.

937 Tan, R., Hendriks, M.A.N., Geiker, M., and Kanstad, T. (2018c). "A numerical investigation of

938   the cracking behaviour of reinforced concrete tie elements." Accepted for publication in the

939   *Magazine of Concrete Research*.

940 Tammo, K., and Thelandersson, S. (2009). "Crack behavior near reinforcing bars in concrete

941   structures." *ACI Structural Journal,* 106(3), 259-267.

942 Watstein, D., and Mathey, R.G. (1959). "Width of Cracks in Concrete at the Surface of

943   Reinforcing Steel Evaluated by Means of Tensile Bond Specimens." *ACI Journal*, 56(7), 47-

944   56.

945 Yannopoulos, P.J. (1989). "Variation of concrete crack widths through the concrete cover to

946   reinforcement." *Magazine of Concrete Research,* 41(147), 63-68.

947

1   **Tables**

2   Table 1. Comparison of crack spacing predicted with mean crack spacing reported in the

3   experiments of Bresler and Bertero (1968) and Yannopoulos (1989), and the FE analysis of Tan

4   et al. (2018c).

	Experimental and FE analysis	Predicted
RC tie	Mean [mm]	Analytical [mm]
Bresler and Bertero (1968)	203	301
Yannopoulos (1989)	90	181
$\phi20c40$	105	224
$\phi32c40$ Tan et al. (2018c)	109	207
$\phi20c90$	260	470
$\phi32c90$	272	434

5

6   Table 2. Comparison of crack spacing predicted with crack spacing reported in the experiments

7   of CEOS.fr (2016) and Tan et al. (2018a).

	Experimental		Predicted
RC tie	Mean [mm]	Maximum [mm]	Analytical [mm]
Tie 4 CEOS.fr (2016)	160	257	370
Tie 5	188	318	370
S-20-40	163	250	422
S-32-40 Tan et al. (2018a)	178	240	361
S-20-90	217	290	422
S-32-90	266	320	361

8

9

10

11

12

13

This is an example created from parts of other articles, it is not designed to be read for sense.

14   Table 3. Comparison of crack spacing reported in the experiments of Tan et al. (2018a) and

15   crack spacing predicted using effective reinforcement ratios.

RC tie	Experimental		Predicted
	Mean [mm]	Maximum [mm]	Analytical [mm]
S-20-40	163	250	390
S-32-40	178	240	342
S-20-90	217	290	422
S-32-90	266	320	361

16

17

Figure

(a)

(b)

Figure

Figure

Figure

(a)

ε

ε_{s0}

ε_s

ε_{ci}

$\varepsilon_s = \varepsilon_{ci}$

x_r

x_s

x

(b)

u

u_0

x_r

x_s

x

(c)

ε

ε_{s0}

ε_s

ε_{ci}

x_s

x

(d)

u

u_0

x_s

x

Figure

(a)

Eq.(39)

(b)

Eq.(40)

Eq.(39)

Figure

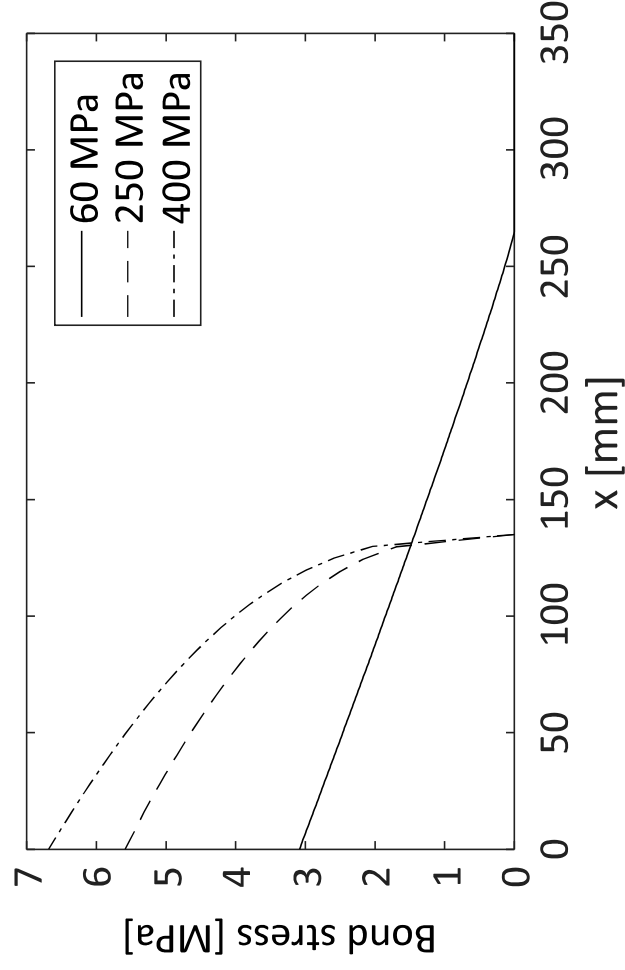(a)

(b)

Figure

(a)

(b)

Figure

(a)

(b)

(c)

(d)

Figure

(a)

(b)

(c)

(d)

(a)

(b)

(c)

(d)

(e)

Figure

(a)

(b)

Figure

Figure to Appendix B

$\varepsilon_{s0,S} > \varepsilon_{s0,cr}$

No — Condition 2

Yes — Condition 1

Condition 2 — $\varepsilon_{s0} < \varepsilon_{s0,S}$

Yes — CLLM

No — CHLM

Condition 1 — $\varepsilon_{s0} < \varepsilon_{s0,cr}$

Yes — CLLM

No — CHLM for $L_{new} = x_{cr}$
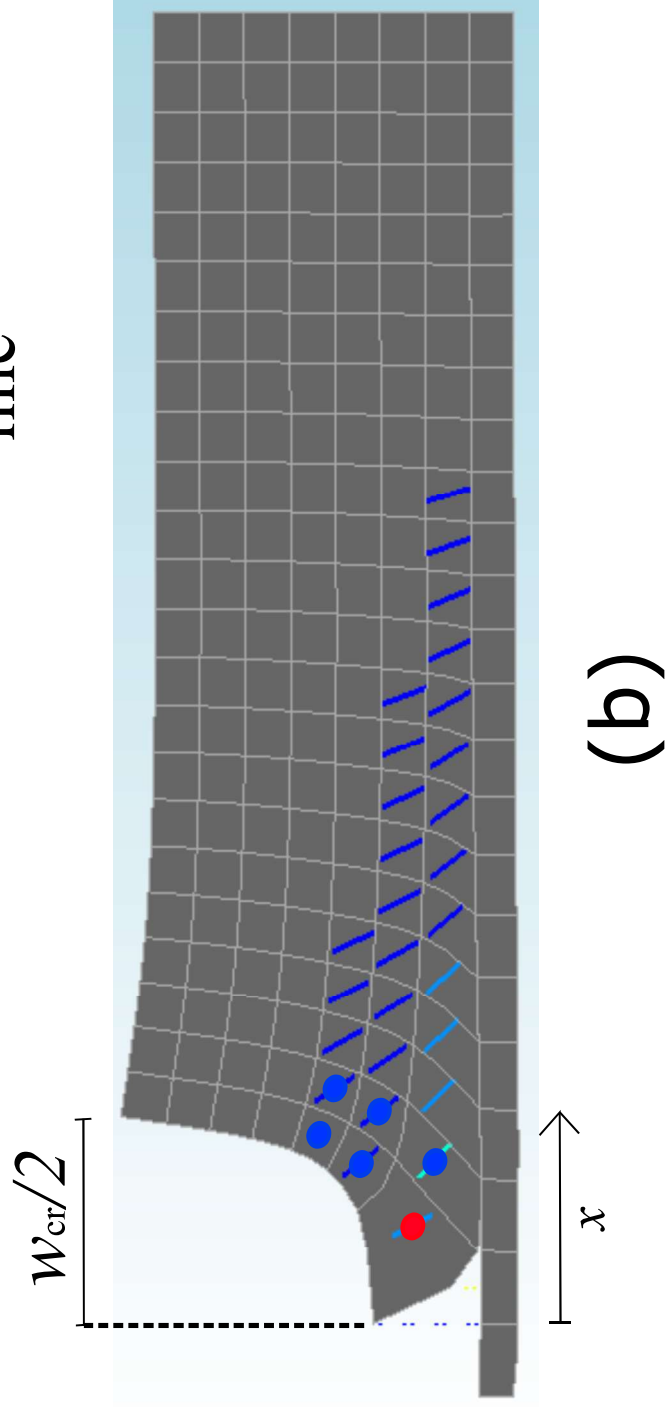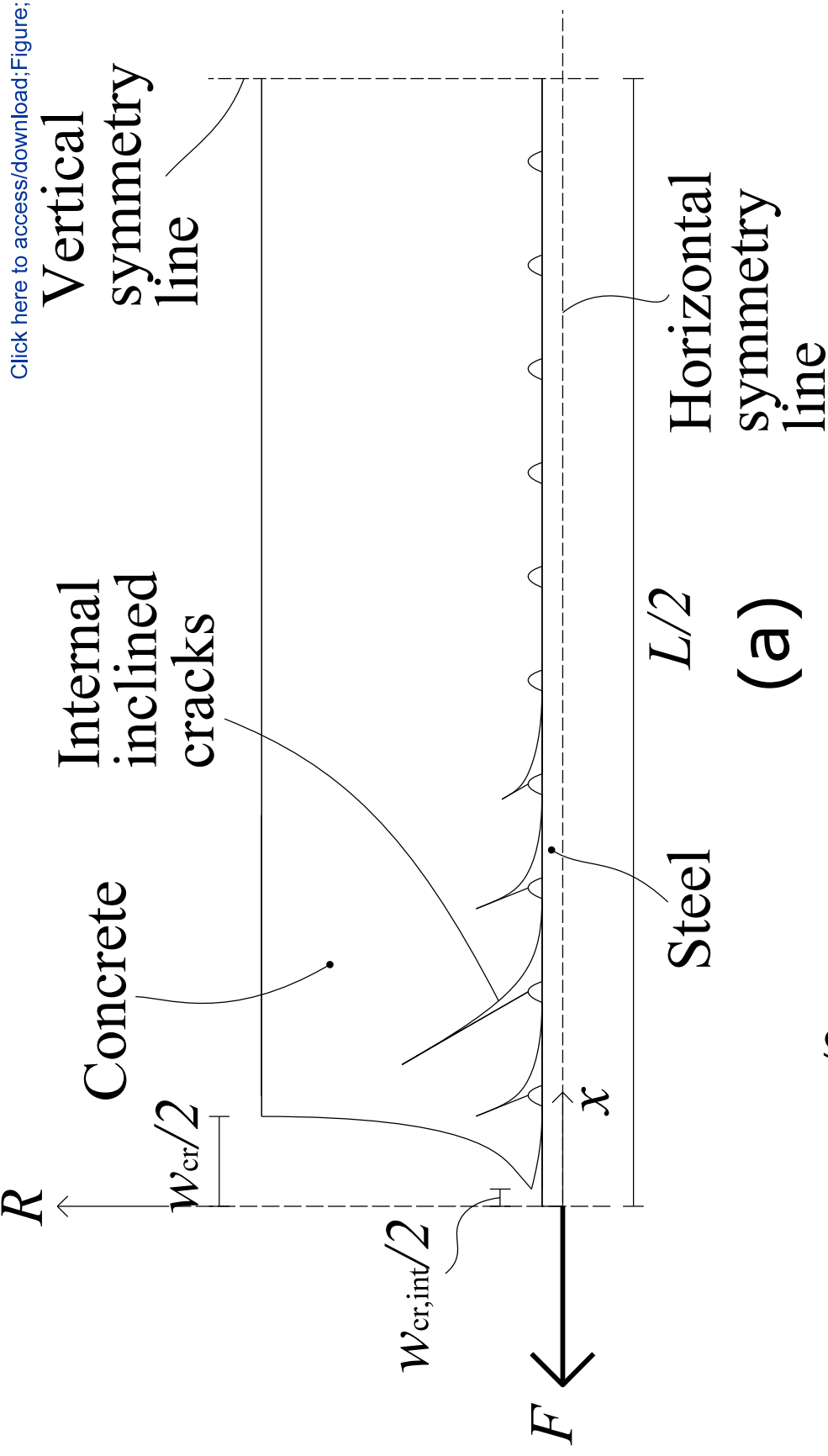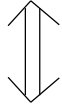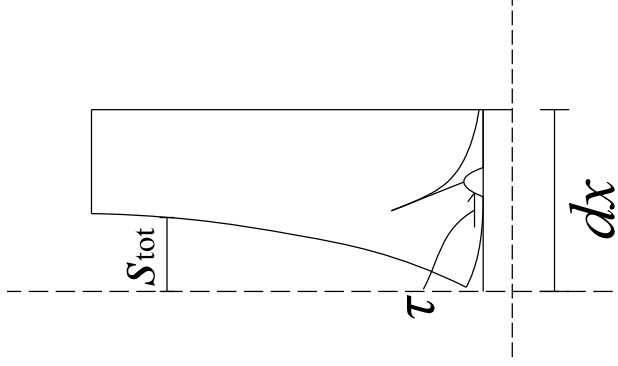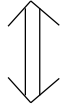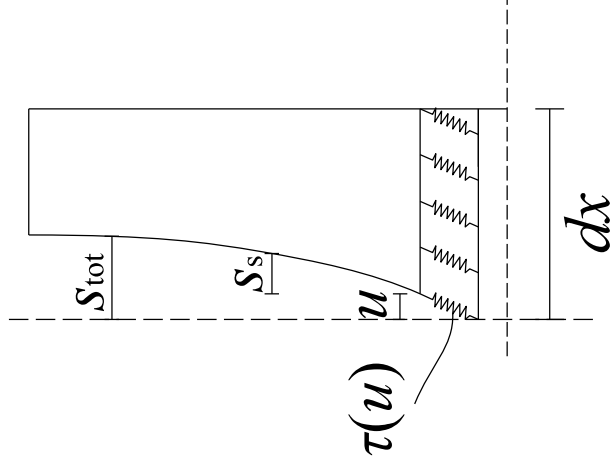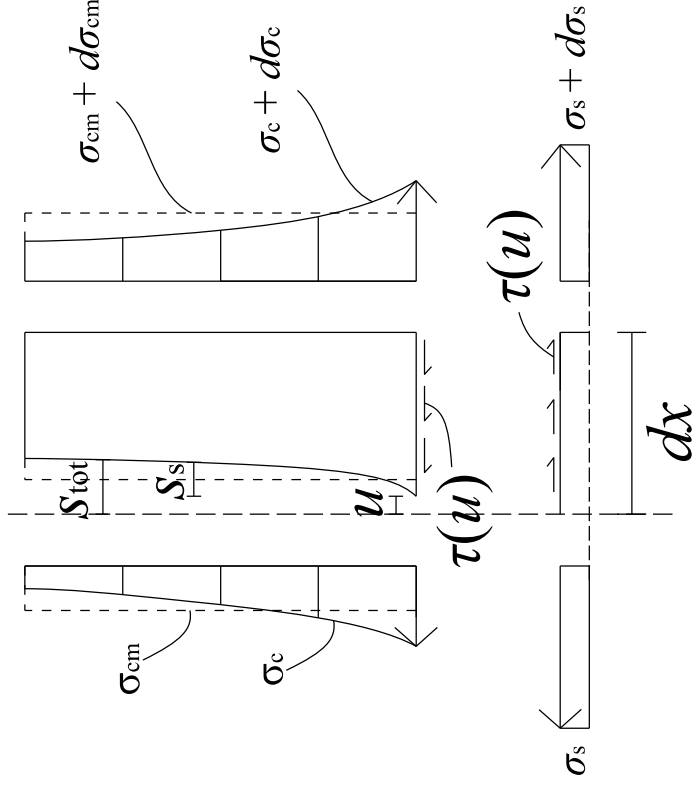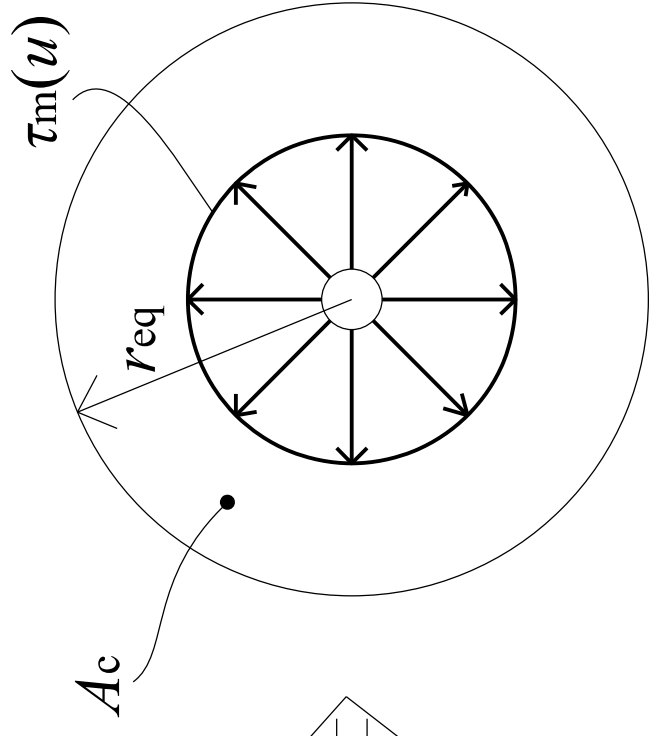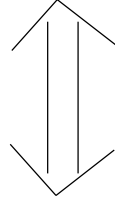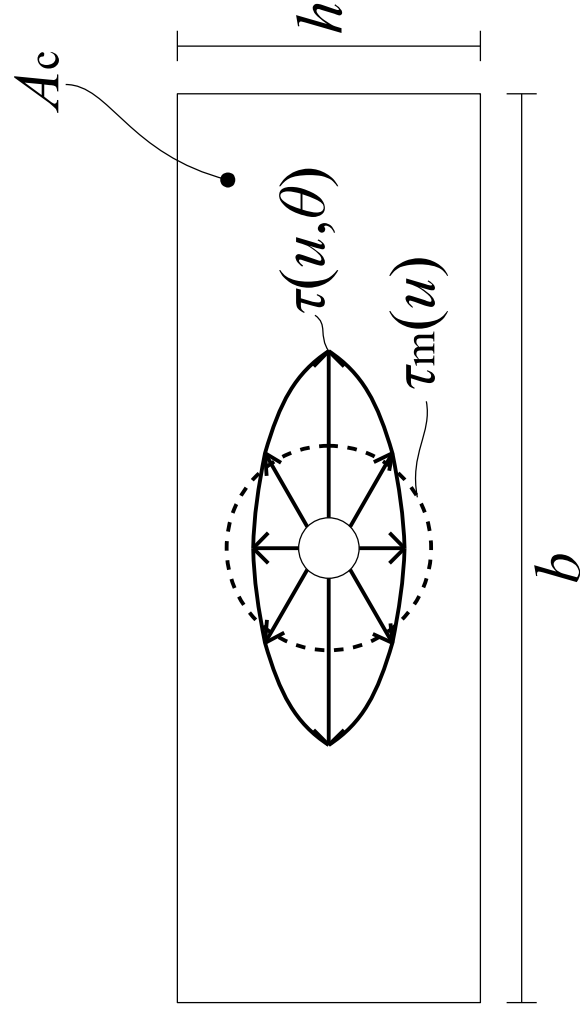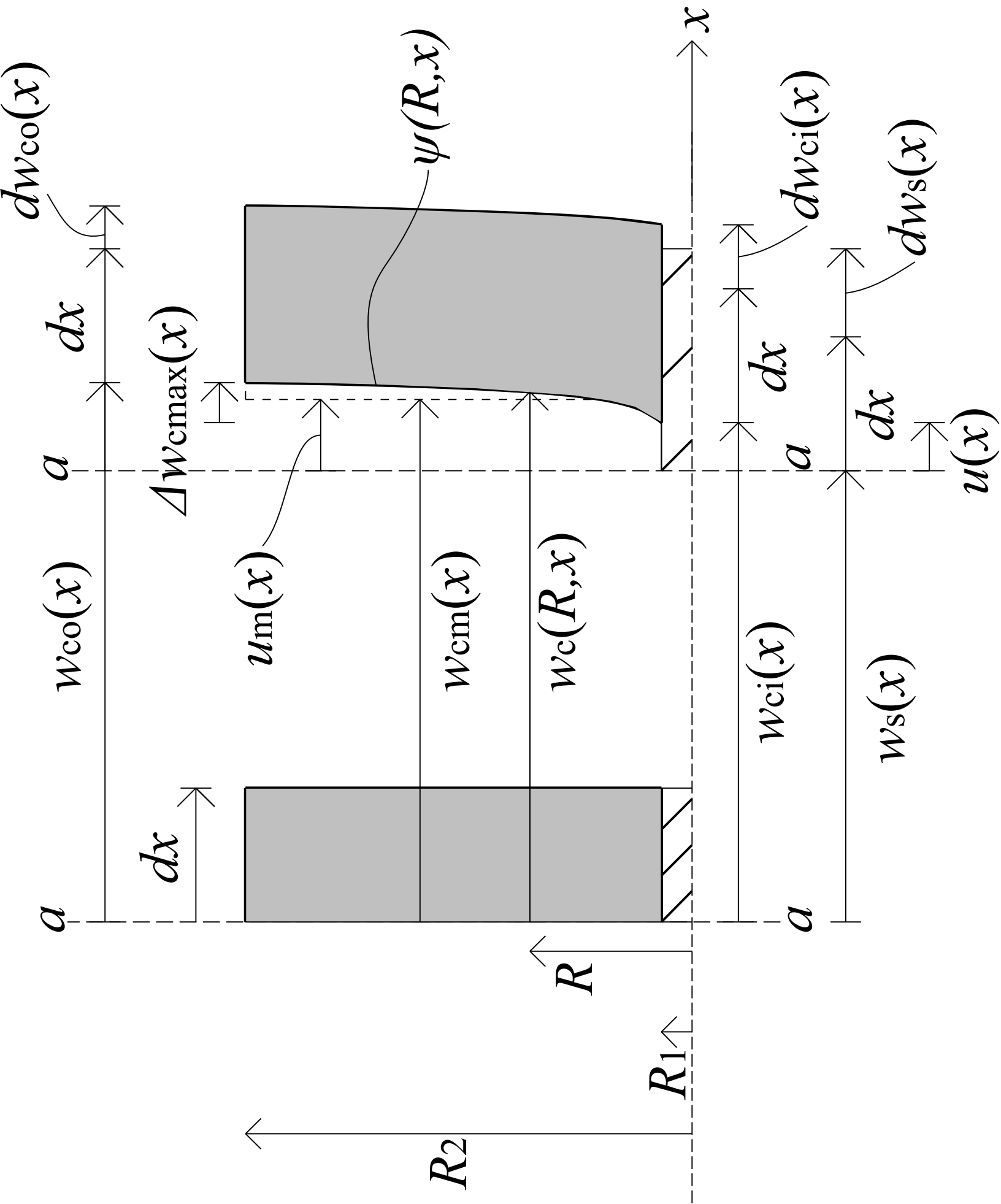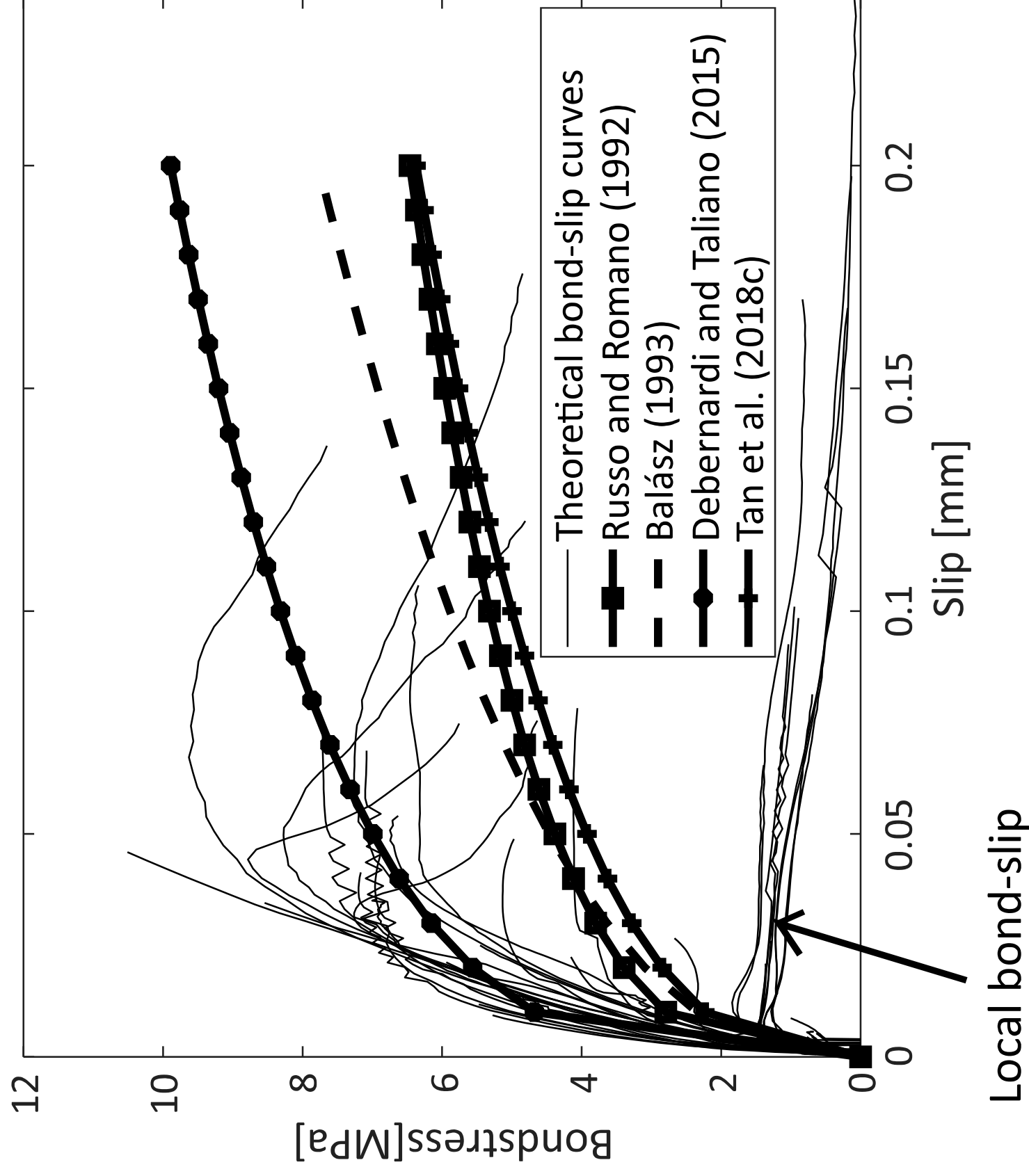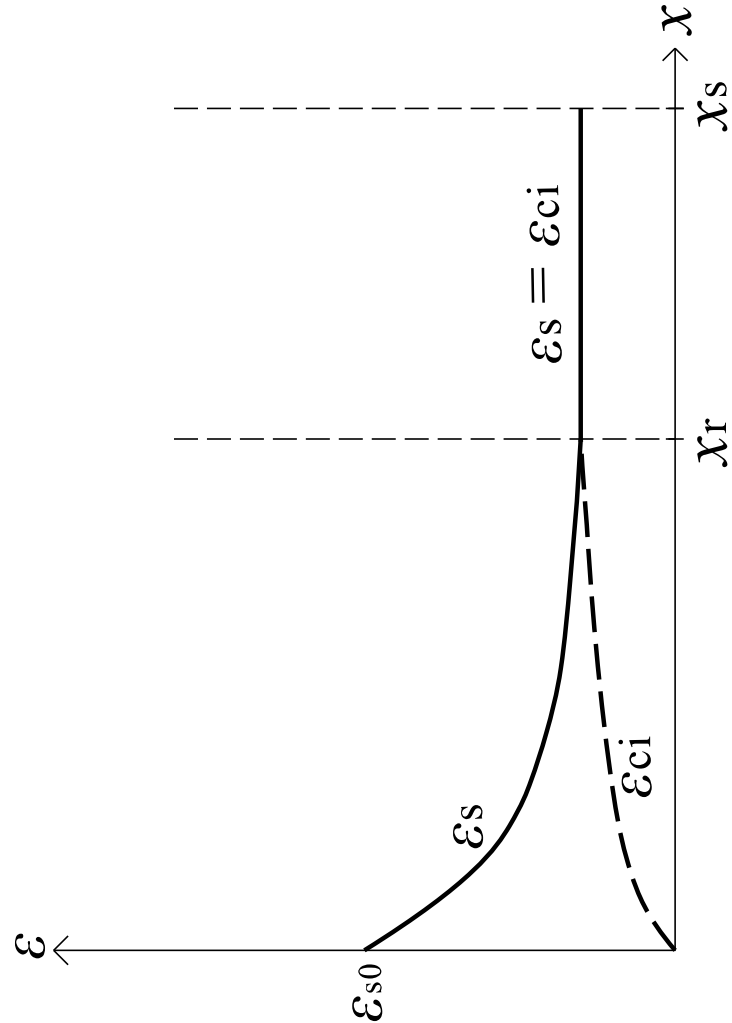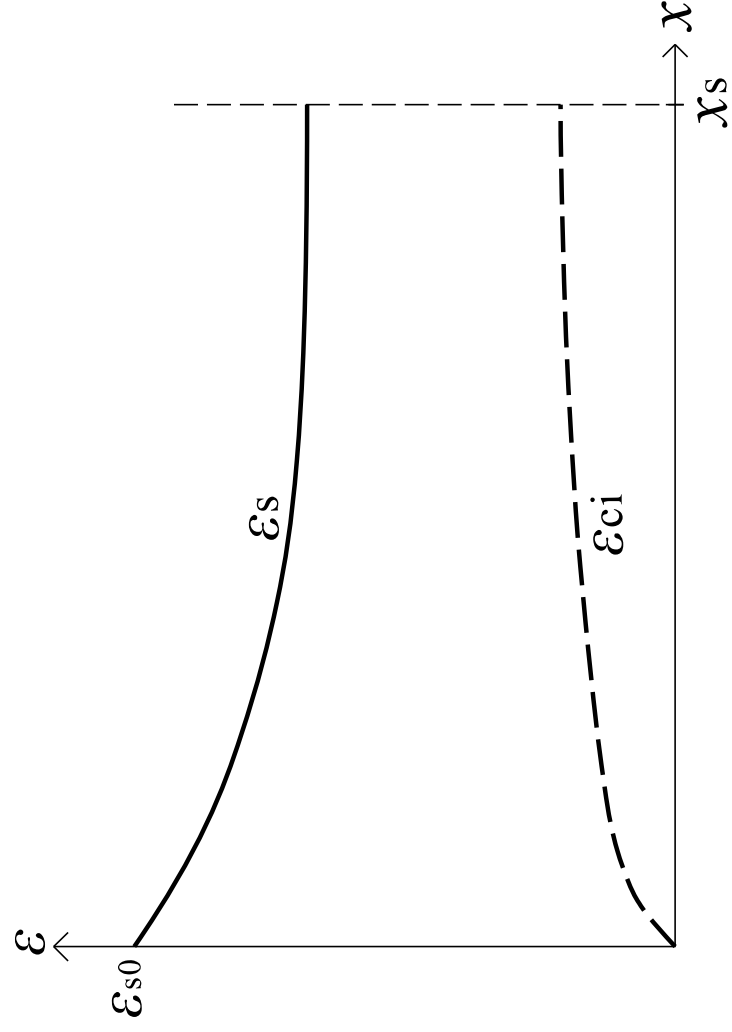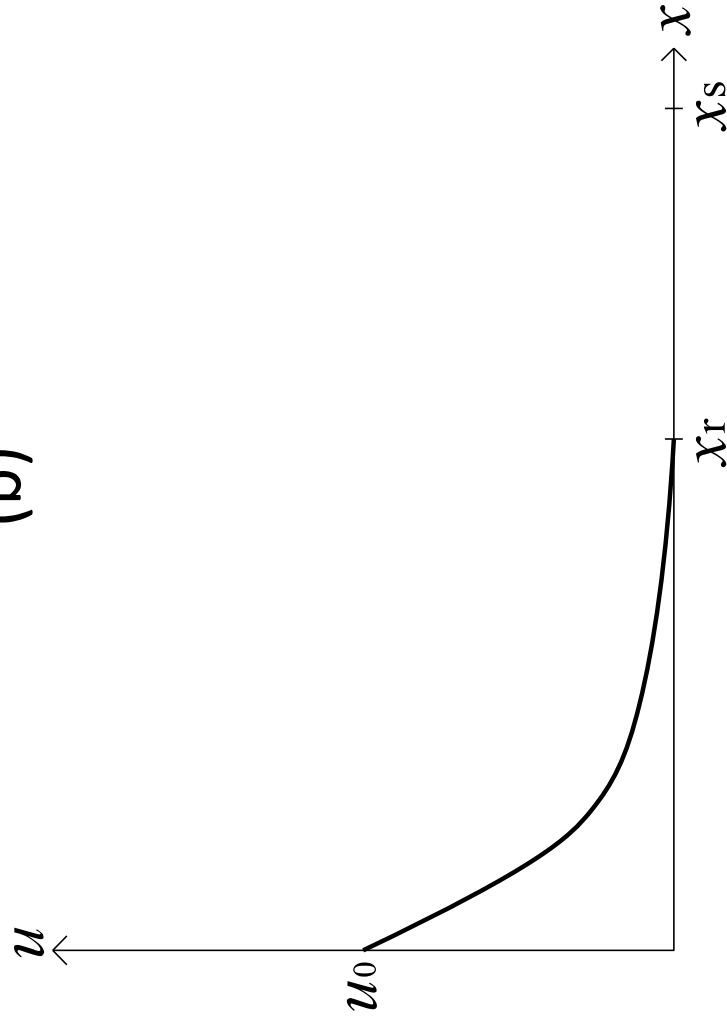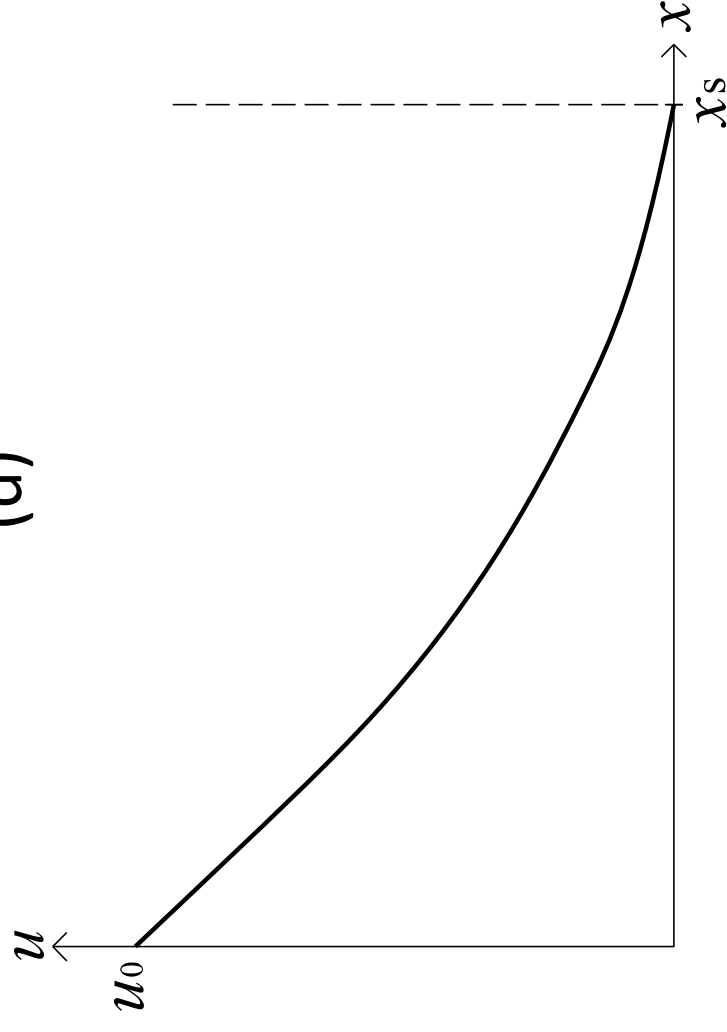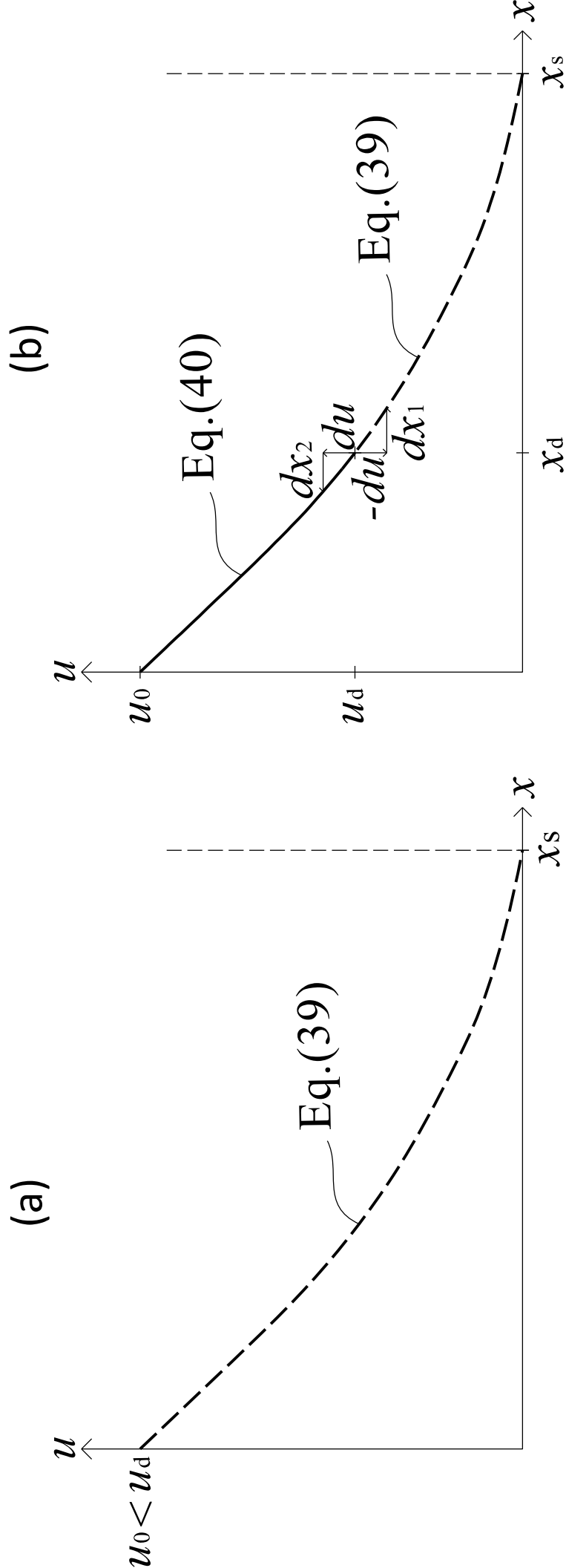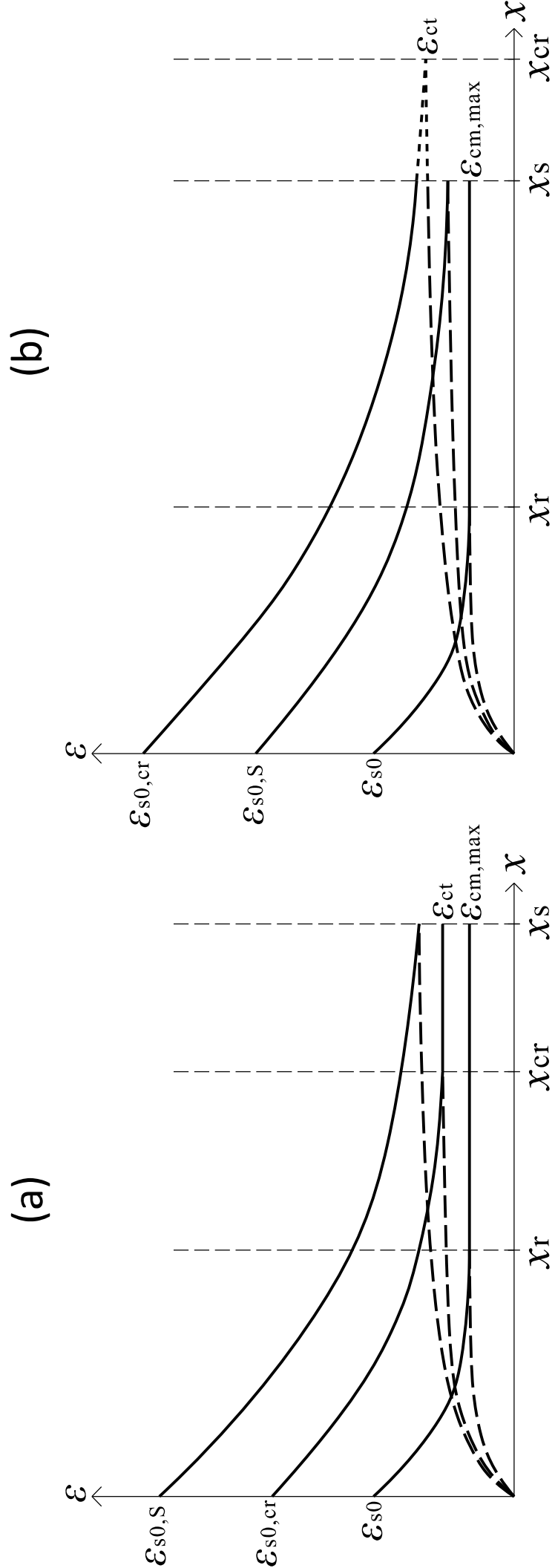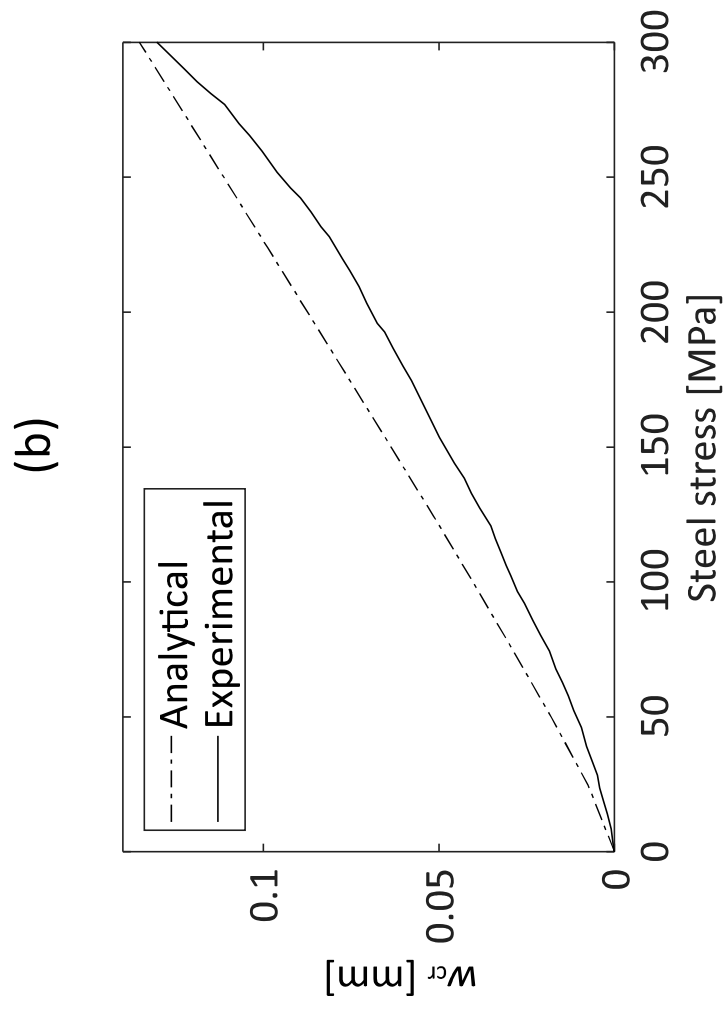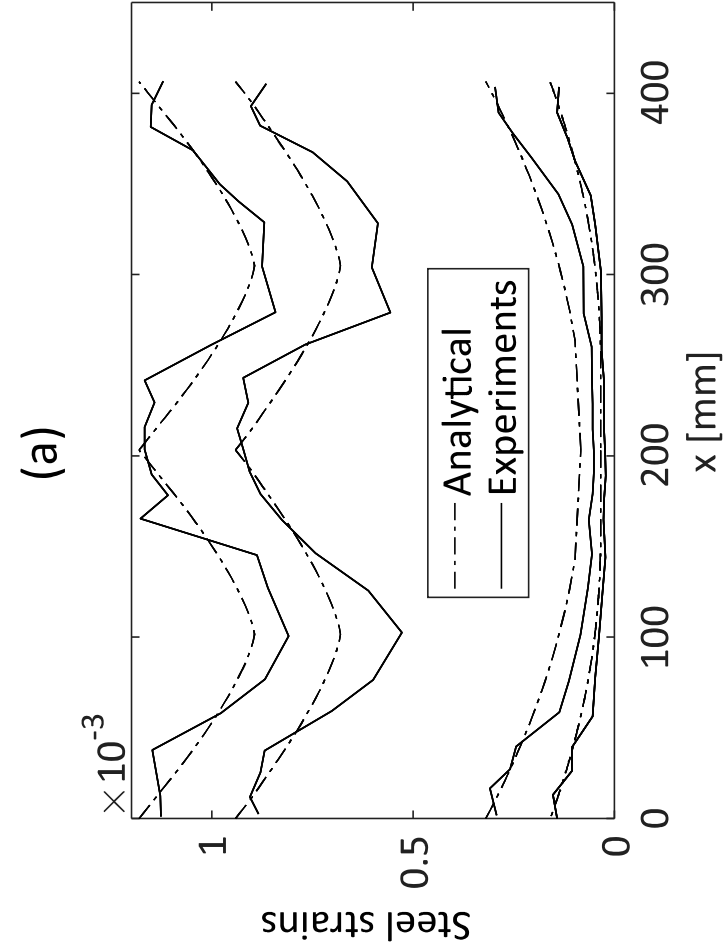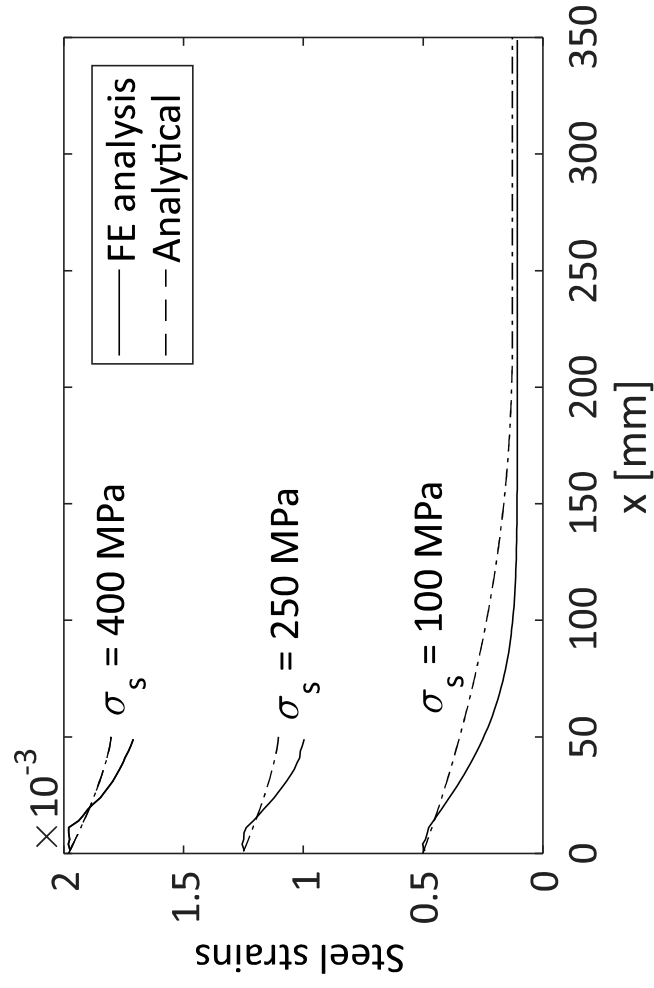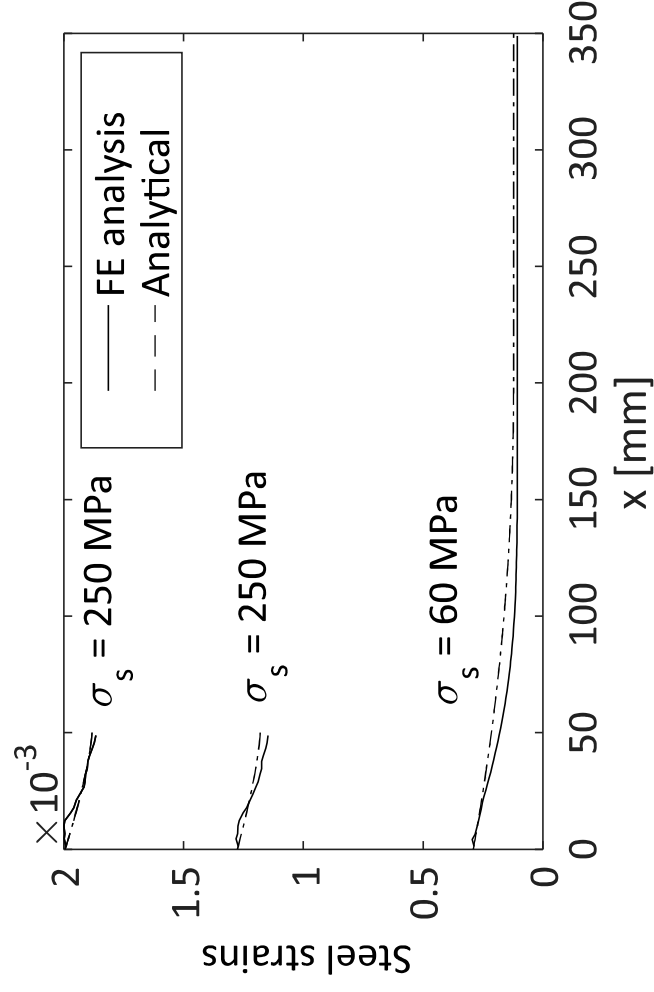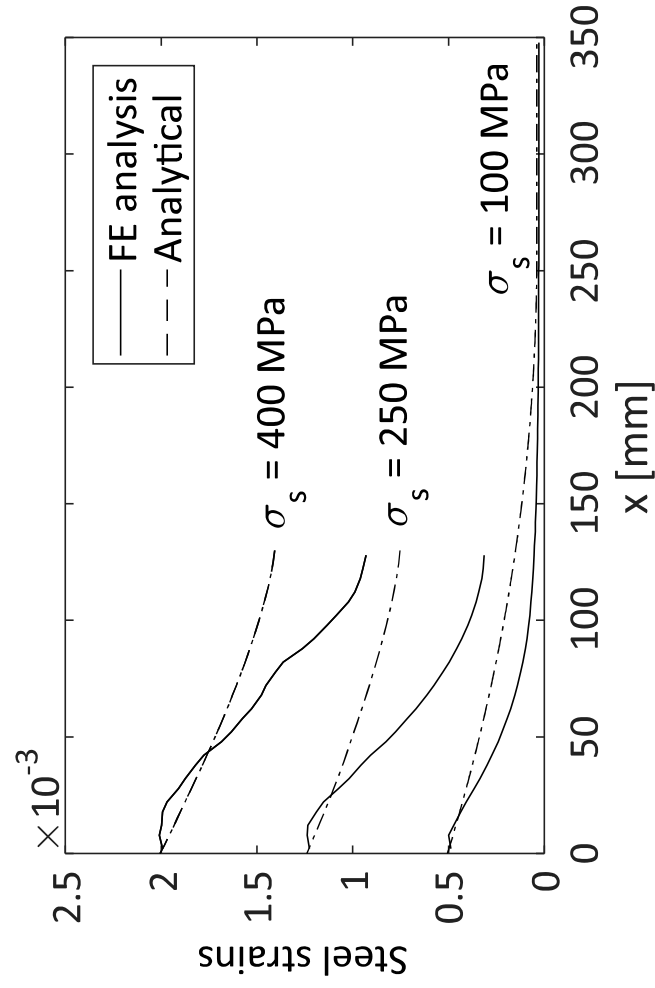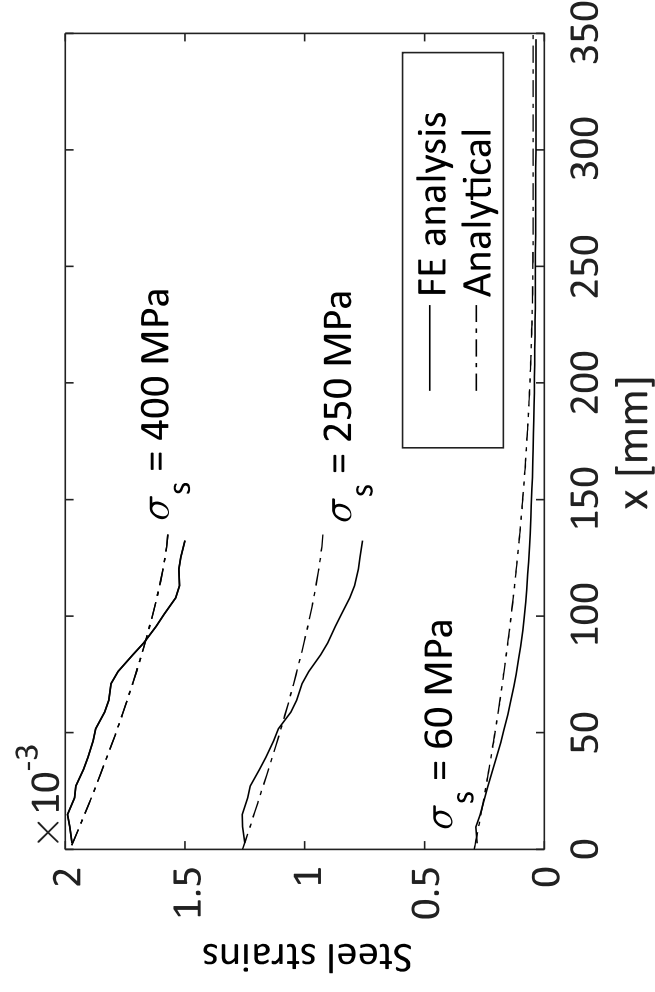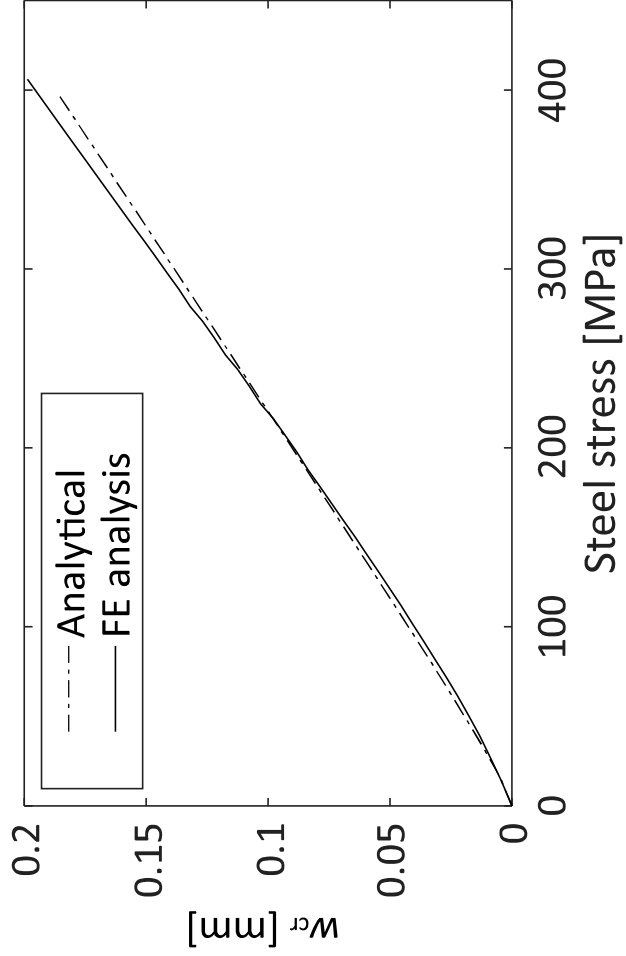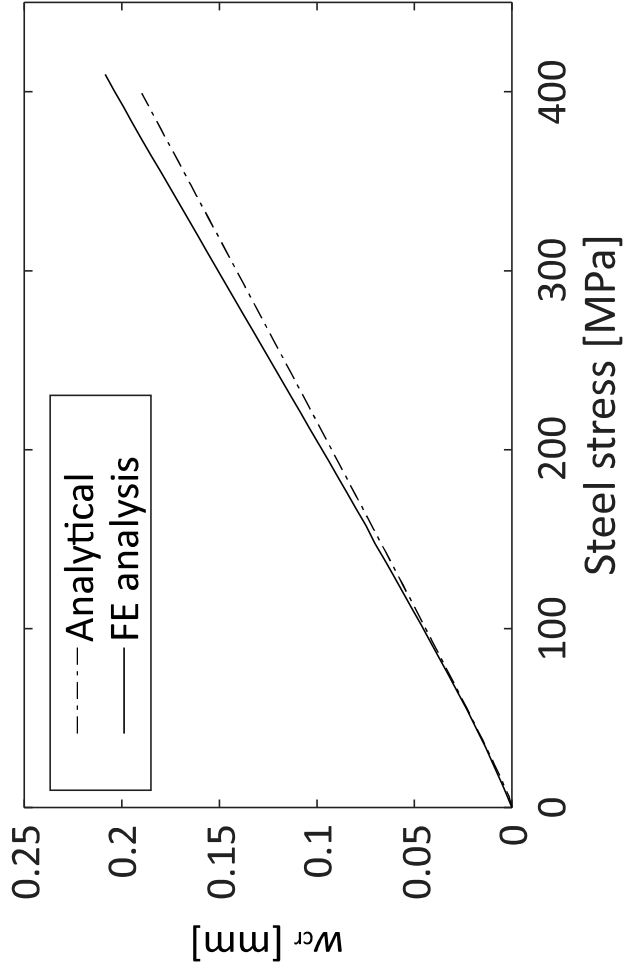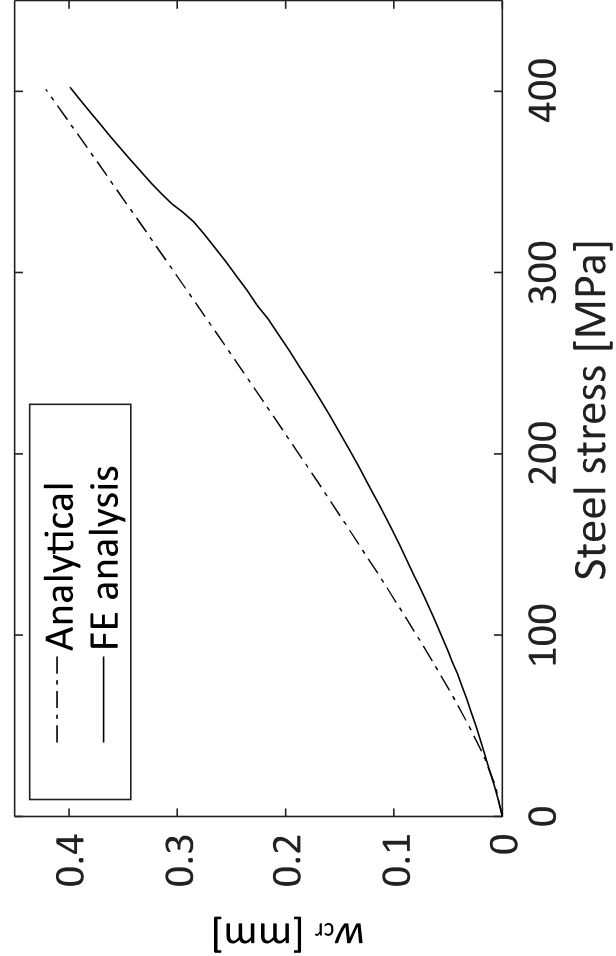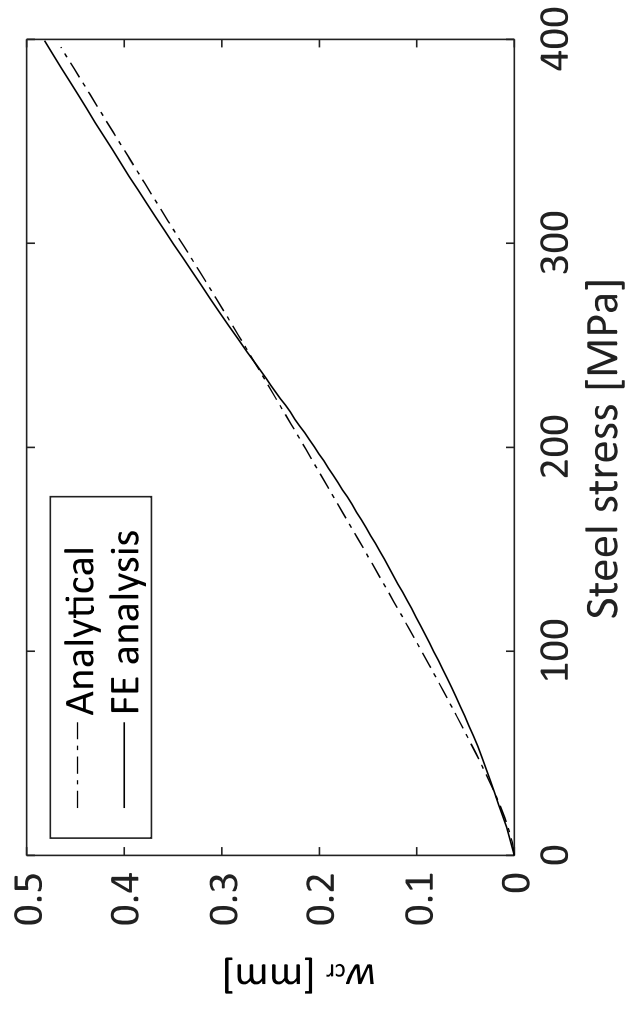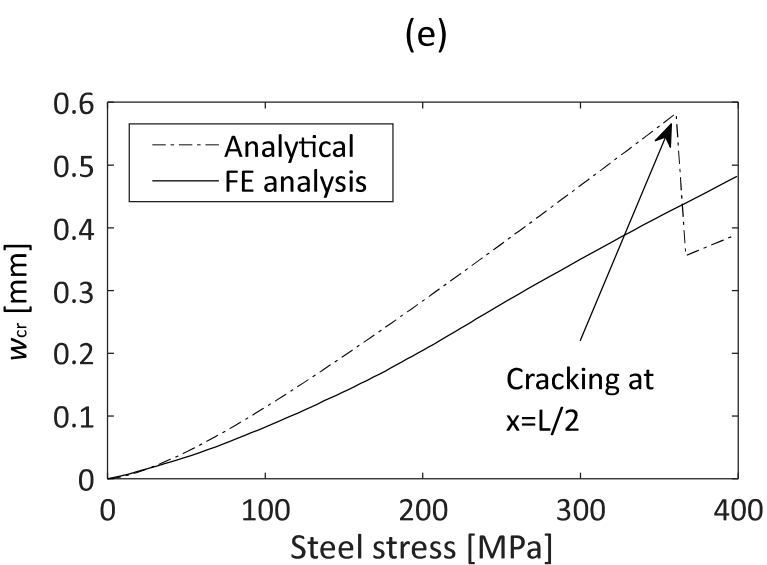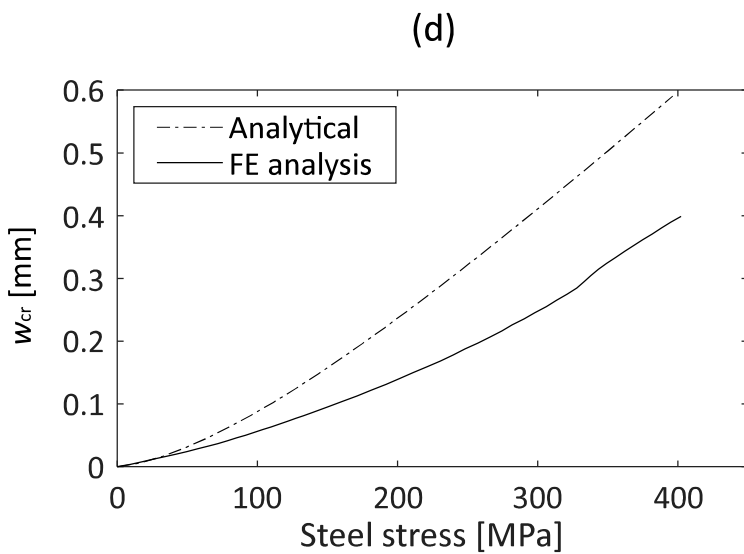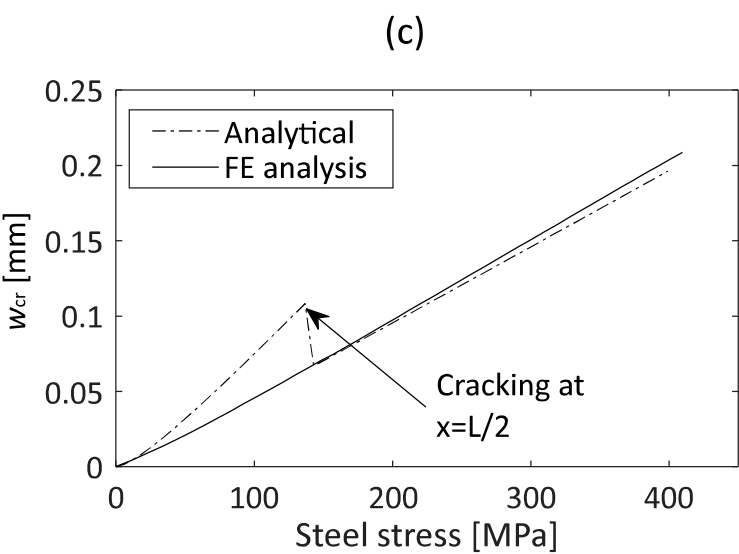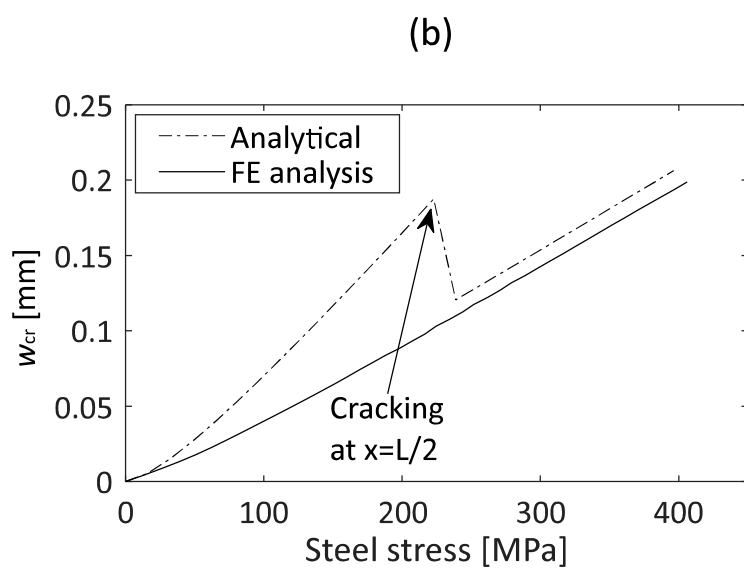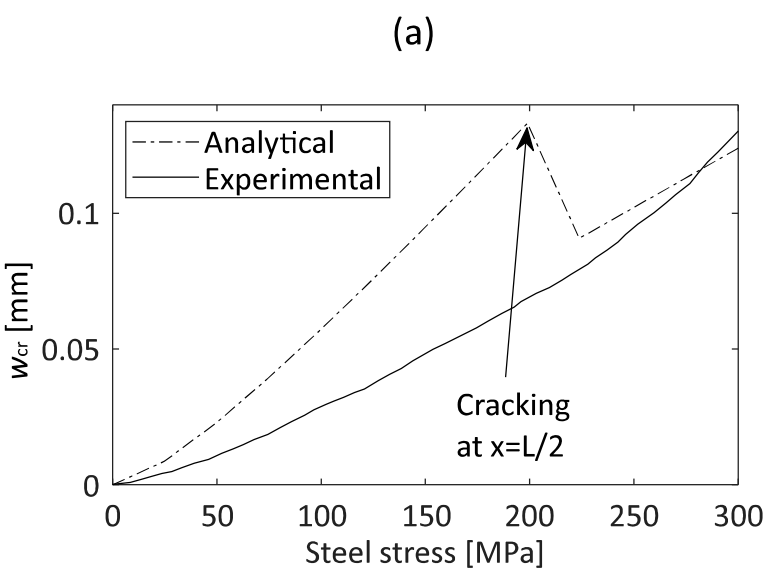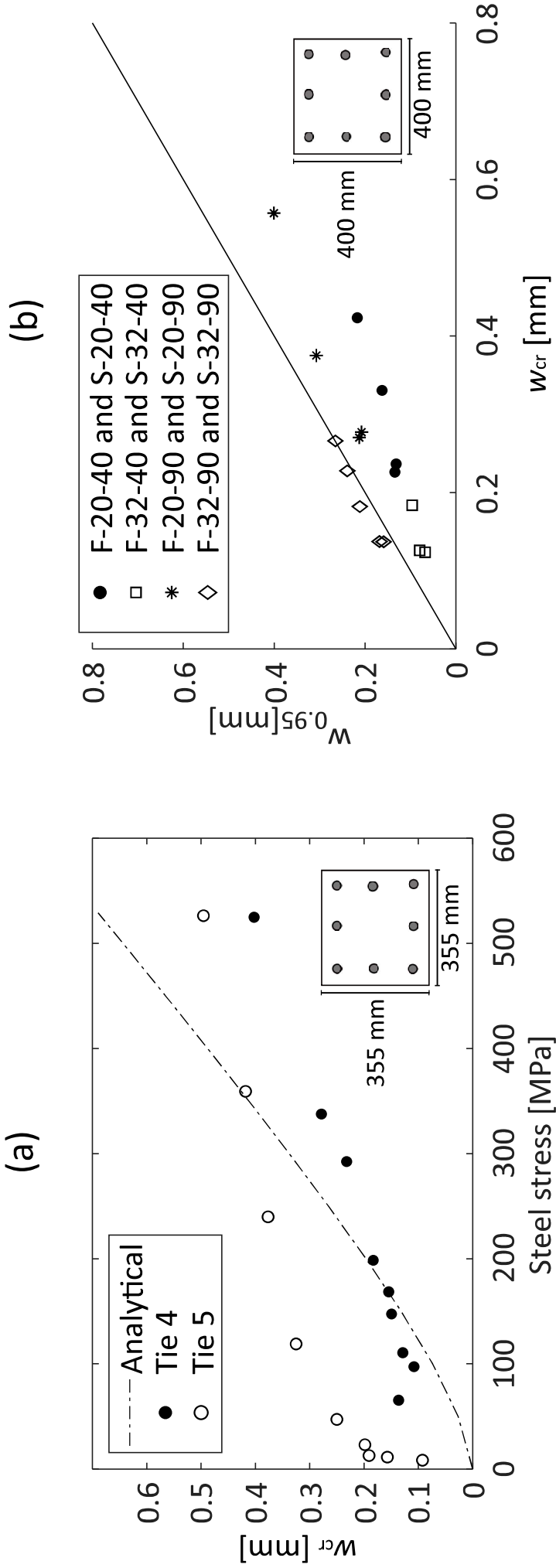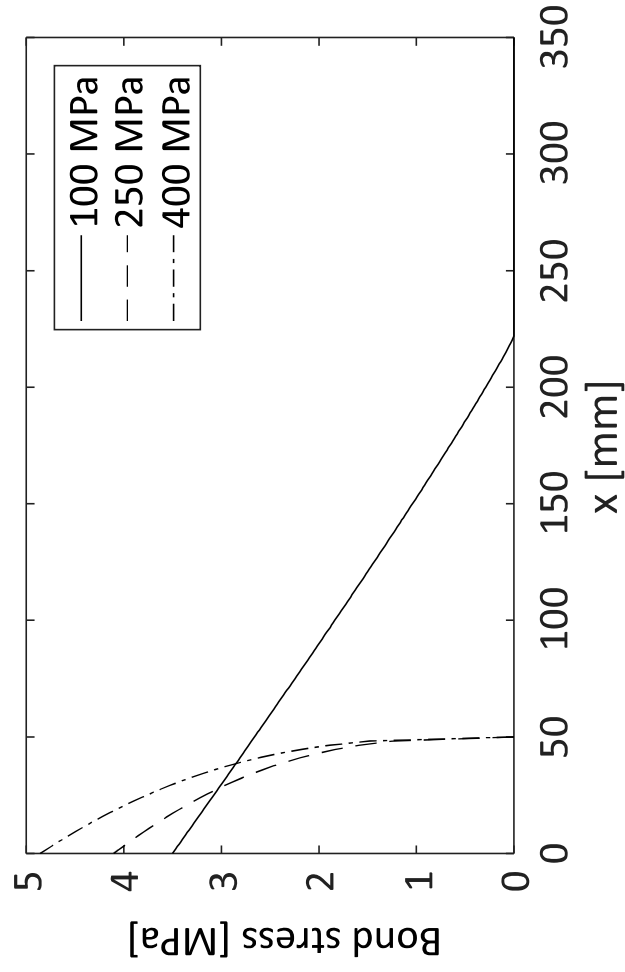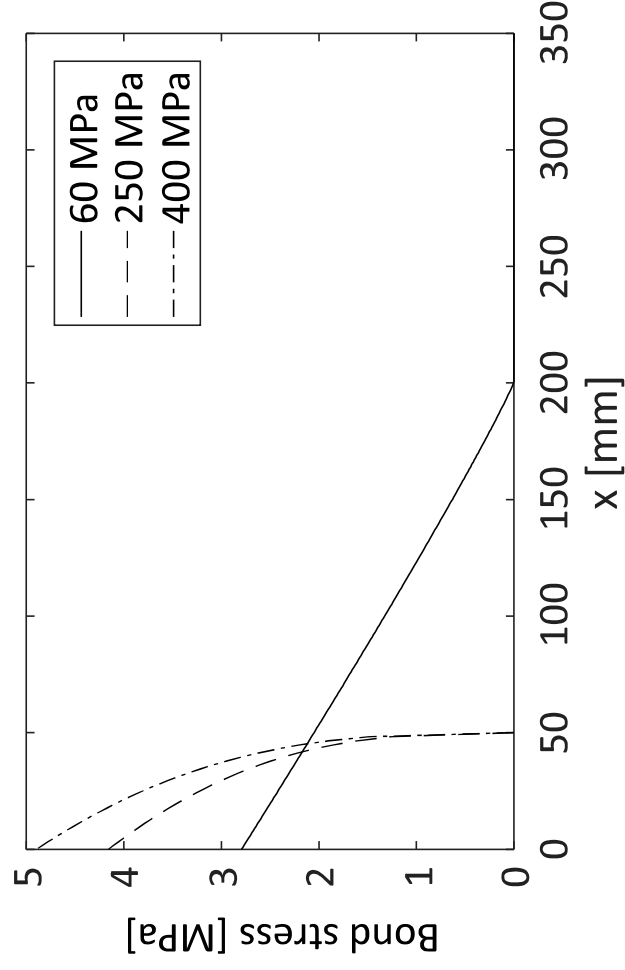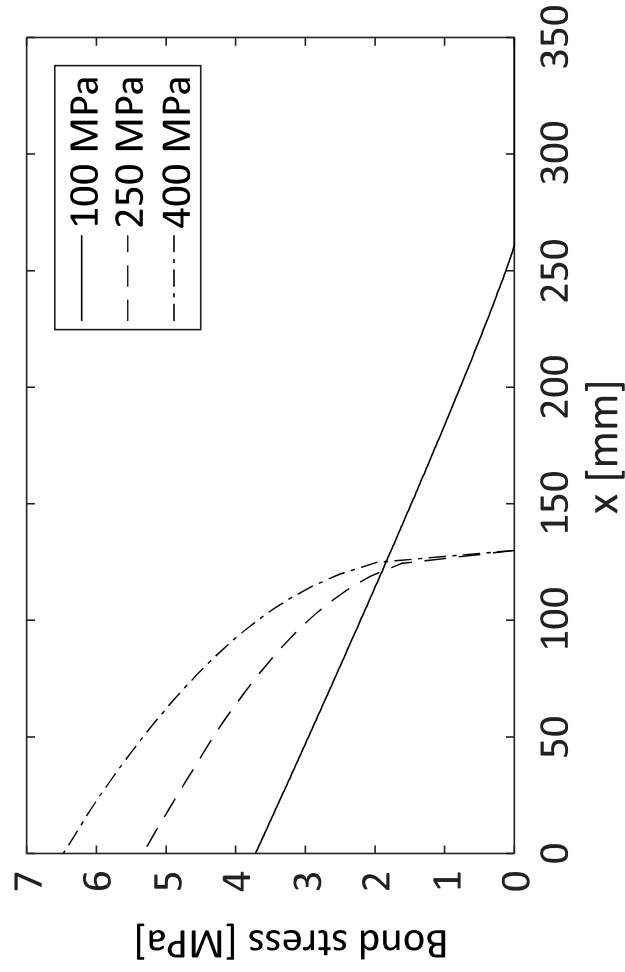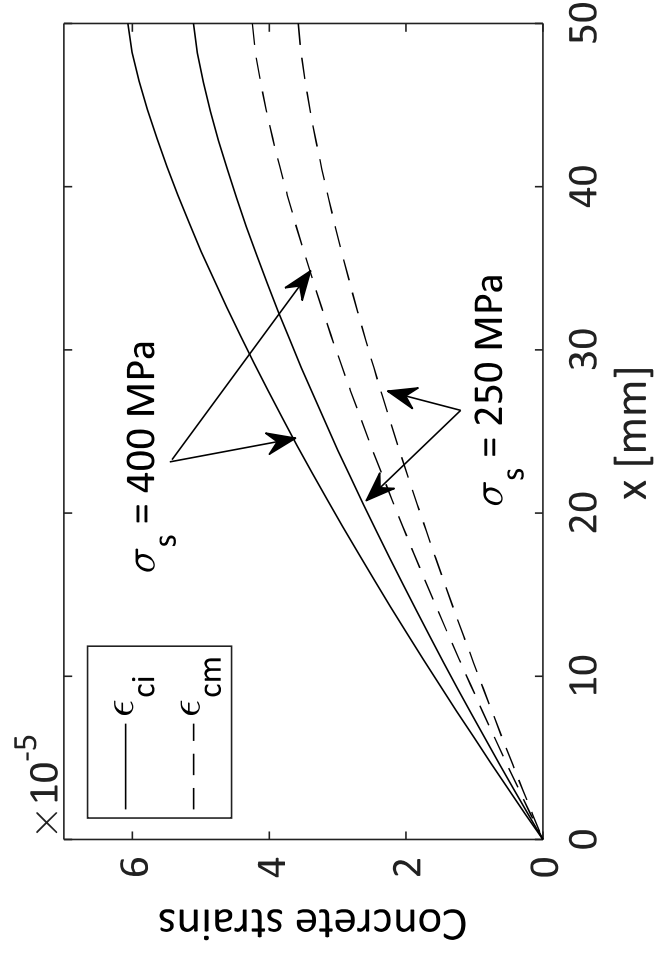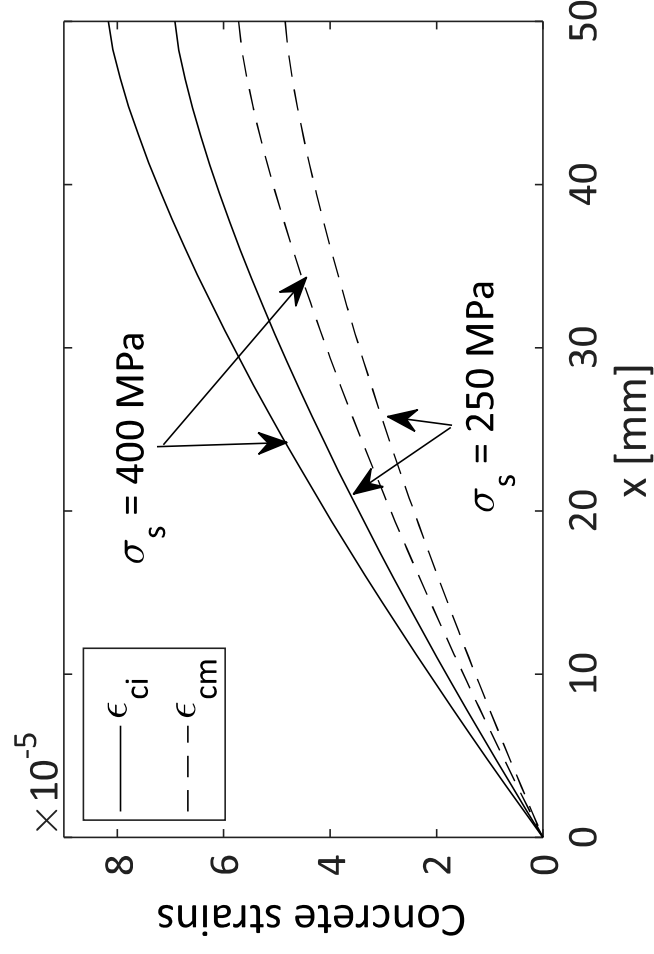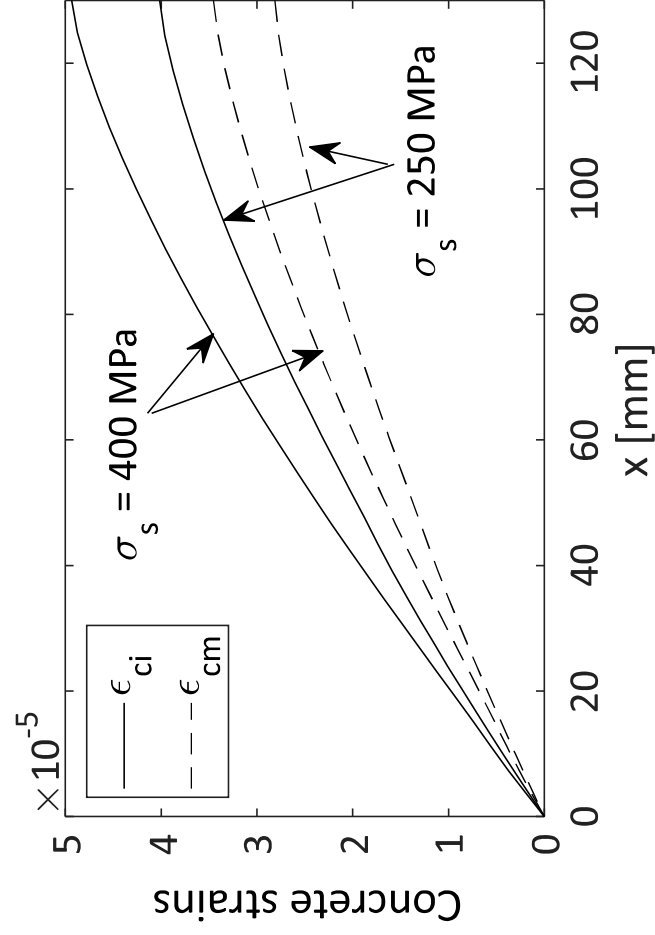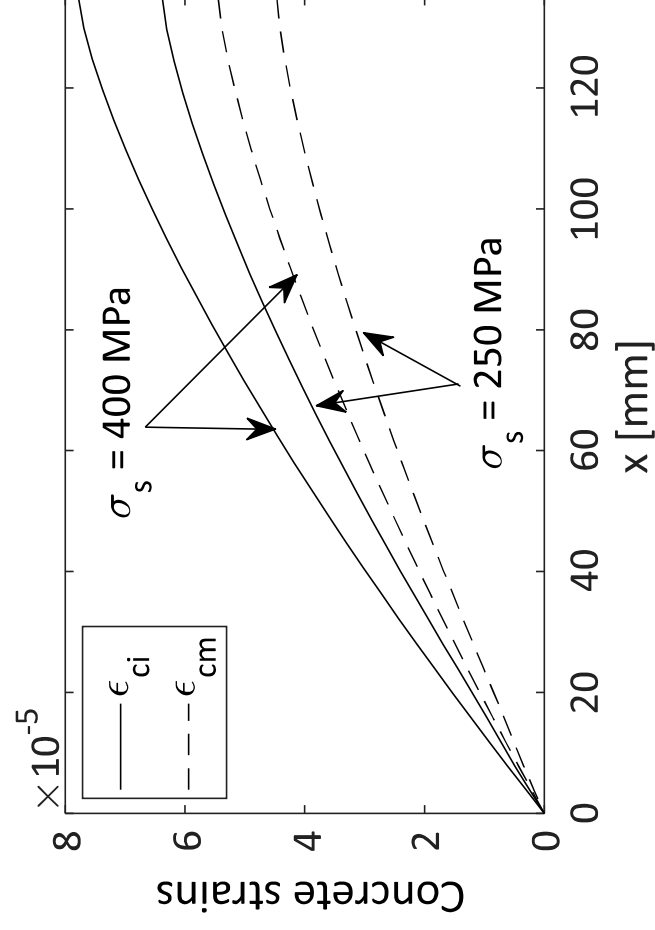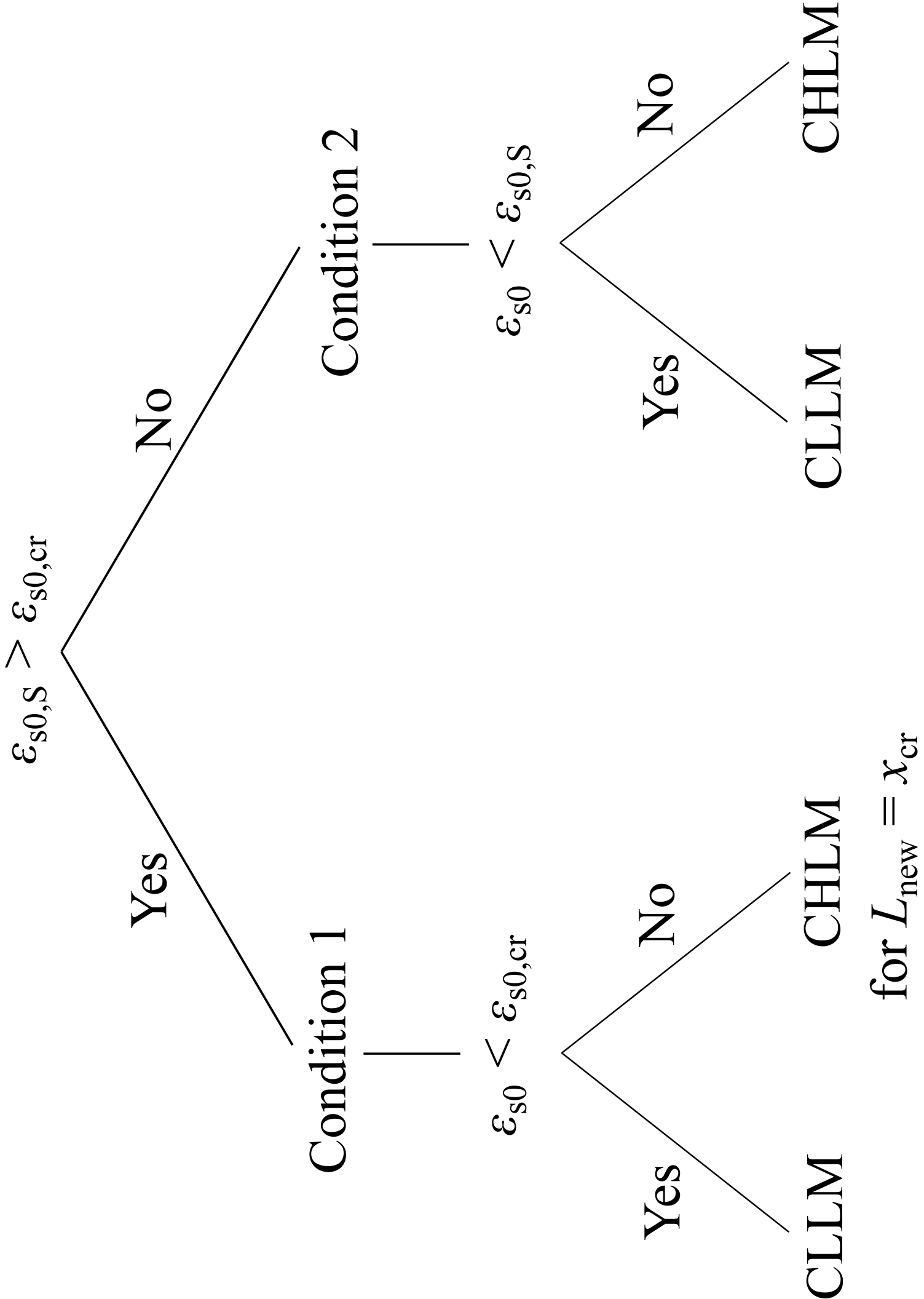
1 **Figures**

2

3 Fig. 1(a) Typical deformation configuration of RC ties with deformed steel bars observed in

4 experiments. (b) FE model with assumptions in accordance with Tan et al. (2018c) showing a

5 typical deformation configuration and crack plot, where straight lines indicate inclined internal

6 cracks and circles indicate internal splitting cracks.

7

8 Figure 2(a) Internally cracked section typically observed in physical experiments. (b) The

9 internal cracking behavior lumped as springs to the interface between concrete and steel. (c)

10 Statically equivalent section using a bond-slip law for the springs. (d) Equivalent cross sections

11 when using the second order differential equation for the slip.

12

13 Figure 3. The displacement field of an arbitrary statically equivalent section. The section to the

14 left hand side shows the undeformed configuration, while the section to the right hand side

15 shows the deformed configuration for a load applied to the rebar end greater than zero.

16

17 Figure 4. Local bond-slip curves according to Eq. (33) with adjusted parameters proposed by

18 Russo and Romano (1992), Balász (1993), Debernardi and Taliano (2015) and Tan et al.

19 (2018c) compared with theoretical local bond-slip curves obtained in the FE analysis of several

20 RC ties at different positions over the bar length in Tan et al. (2018c).

21

22 Figure 5(a) and (b) Strain and slip distribution in CLLM. (c) and (d) Strain and slip distribution in

23 CHLM.

24

25 Figure 6(a) Case 1: solution for the slip using Eq. (39), i.e. $u_0 < u_d$. (b) Case 2: solution for the

26 slip using Eq. (39) for $0 < u < u_d$ and Eq. (40) for $u_d < u < u_0$.

27

28 Figure 7(a) Condition 1. (b) Condition 2.

29

This is an example created from parts of other articles, it is not designed to be read for sense.

30   Figure 8(a) Comparison of steel strains predicted with steel strains reported in the experiments

31   of Bresler and Bertero (1968) over the bar length. (b) Comparison of crack widths predicted with

32   crack widths reported in the experiments of Yannopoulos (1989) using similar specimen length

33    $L = 100$ mm similar to that in the experiments.

34

35   Figure 9. Comparison of steel strains predicted with steel strains reported over the bar length in

36   the FE analysis of Tan et al. (2018c). (a) Specimen $\phi20c40$. (b) Specimen $\phi32c40$. (c)

37   Specimen $\phi20c90$. (d) Specimen $\phi32c90$.

38

39   Fig. 10. Comparison of crack widths predicted (in specimens with lengths similar to FE analysis

40   mean crack spacing reported in Table 1) with crack widths reported in the FE analysis of Tan et

41   al. (2018c). (a) Specimen $\phi20c40$, $L = 105$ mm. (b) Specimen $\phi32c40$, $L = 109$ mm. (c)

42   Specimen $\phi20c90$, $L = 260$ mm. (d) Specimen $\phi32c90$, $L = 272$ mm.

43

44   Fig. 11. Comparison of crack widths predicted (in specimens with lengths similar to crack

45   spacing predicted in Table 1) with crack widths reported in the experiments of Yannopoulos

46   (1989) and the FE analysis of Tan et al. (2018c). (a) Yannopoulos (1989) specimen, $L =$

47   181 mm. (b) Specimen $\phi20c40$, $L = 224$ mm. (c) Specimen $\phi32c40$, $L = 207$ mm. (d) Specimen

48    $\phi20c90$, $L = 470$ mm. (e) Specimen $\phi32c90$, $L = 434$ mm.

49

50   Fig. 12. Comparison of crack widths predicted (in specimens with lengths similar to crack

51   spacing predicted in Table 2) with crack widths reported in experiments. (a) CEOS.fr (2016). (b)

52   Tan et al. (2018a).

53

54   Fig. 13. Bond stresses corresponding to the steel strains predicted in Fig. 9. (a) Specimen

55    $\phi20c40$. (b) Specimen $\phi32c40$. (c) Specimen $\phi20c90$. (d) Specimen $\phi32c90$.

56

57   Fig. 14. Concrete strains corresponding to the steel strains predicted in Fig. 9. (a) Specimen

58    $\phi20c40$. (b) Specimen $\phi32c40$. (c) Specimen $\phi20c90$. (d) Specimen $\phi32c90$.

59